A Comparison of Rotor Disk Modeling and Blade-Resolved CFD Simulations for NASA's Tiltwing Air Taxi

David Garcia Perez **Patricia Ventura Diaz**
Science and Technology Corporation
NASA Ames Research Center
Moffett Field, California, USA

Jasim Ahmad **Seokkwan Yoon**
NASA Advanced Supercomputing Division
NASA Ames Research Center
Moffett Field, California, USA

ABSTRACT

A multi-fidelity computational fluid dynamics analysis is carried out for NASA's tiltwing air taxi concept operating in airplane and helicopter mode. High-fidelity simulations are computationally expensive due to individual rotor blade modeling in a time-dependent computational domain with rotating grids. The mid-fidelity rotor disk option, in its source term implementation, is explored as a more affordable alternative. Computations are performed with NASA's OVERFLOW flow solver loosely-coupled with the comprehensive code CAMRAD II for appropriate rotor trim. Detailed comparisons are shown for the trim solution, airloads, wake geometry, and rotor performance. While the rotor disk model is able to capture the flow field with satisfactory agreement in airplane mode, it faces difficulties in helicopter mode due to the three-dimensional effects of the wake. Although this study is limited to a specific vehicle geometry, it is expected that the results are somewhat generalizable to the analysis of multi-rotor configurations.

NOTATION

Greek symbols

Symbol	Description
α	Angle of attack
β_0	Coning angle
β_{1c}	Longitudinal flapping angle
β_{1s}	Lateral flapping angle
η	Propulsive efficiency
Ω	Rotor rotational speed
ϕ	Inflow angle
ψ	Azimuth position
ρ	Fluid density
θ_0	Collective pitch angle

Roman symbols

Symbol	Description
a	Fluid speed of sound
c	Local rotor blade chord length
FM	Figure of merit
F_x	Horizontal force in airframe axes
F_z	Vertical force in airframe axes
h	Flight altitude
M	Mach number
M^2c_c	Sectional chord force coefficient
M^2c_m	Sectional pitching moment coefficient
M^2c_n	Sectional normal force coefficient
M_y	Pitching moment in airframe axes
P	Rotor power
R	Rotor radius
r	Radial position
T	Rotor thrust
V_∞	Freestream velocity
v_i	Induced velocity
y^+	Non-dimensional viscous wall spacing

Subscripts

Subscript	Description
∞	Freestream
root	Blade root
tip	Blade tip

Presented at the Vertical Flight Society's 79th Annual Forum & Technology Display, West Palm Beach, FL, USA, May 16–18, 2023.

INTRODUCTION

In the past years, the rapid expansion of the urban air mobility (UAM) industry has sparked interest in multirotor configurations, as an alternative to conventional helicopters, to fly passengers and cargo over urban and suburban areas. NASA, in a joint effort with industry partners and academia, is working on the development and support of emerging aviation markets. As part of the Revolutionary Vertical Lift Technology (RVLT) project, NASA has established a fleet of conceptual vehicles for air taxi operations. Proposed geometries include a quadrotor, a side-by-side helicopter, a lift+cruise configuration, a quiet single-main rotor helicopter, and a tiltwing vehicle (Ref. 1).

Characterization of the multirotor flow field and interactional aerodynamics around these rotorcraft still constitutes a challenging task. Aerodynamic phenomena influencing the rotor are multiple and very difficult to predict. The flow field is inherently unsteady and dominated by vortical structures in the wake. Blade-vortex interactions (BVI) occur near the rotor when a passing blade encounters tip vortices shed by previous blades. Advancing rotor blades may experience transonic flow whereas retreating blades may suffer from dynamic stall and boundary layer separation. Lower Reynolds numbers present in multiple rotor flows pose a different challenge in predicting the boundary layer transition and thus the aerodynamic loads. The lessons learned from conventional helicopters are still applicable, where complex fluid-structure interactions play a major role in performance, vibratory loads, and noise emissions. In multirotor configurations, additionally, interactional aerodynamics effects become a major factor in performance prediction. Even with the computational resources available today, it remains arduous to solve the fully-resolved rotor aeromechanic problem, incorporating the complexity of all the related processes into the calculations. Previous high-fidelity computational fluid dynamics (CFD) work by Ventura Diaz et al. (Refs. 2–4) on NASA's urban air taxi concepts demonstrated that high-fidelity methods are the right tool to analyze their performance while capturing the relevant flow features and aerodynamic interactions. These simulations are routinely performed on powerful supercomputers using overset moving grids, and a coupled CFD and comprehensive analysis utilizing computational structural dynamics (CSD) (Refs. 5, 6). However, their use is often impractical in the preliminary stages of design, where the final geometry has not been established yet.

To overcome this problem, one can resort to simplified methods that incur less computational costs at the expense of sacrificing accuracy. Since its conception, the actuator disk has become a very popular technique to model rotor influence and reproduce the rotor installation effects. In its general form, this model treats the rotor as an infinitely thin, permeable disk that sustains a pressure jump. Some formulations allow to retain an unsteady framework while the computational cost is relaxed on the grid generation side. For example, Boyd (Ref. 7) developed an unsteady pressure jump boundary condition by coupling the generalized dynamic wake theory with a Navier-Stokes solution procedure. For the first time, unsteady pressures on the fuselage sidelines matched well with experimental data. More restrictive assumptions yield a time-averaged representation of the flow. Several authors (Refs. 8–10) have demonstrated the ability of the rotor disk model to predict the mean characteristics of the flow field, and rotor-wing or rotor-fuselage interactions in hover and forward flight. However, some models failed to predict separation regions and severe suction zones. More recently, Ahmad (Ref. 11) proposed an alternative loose CFD/CSD coupling using OVERFLOW/CAMRAD II valid for the disk model approximation. For multirotor configurations, the turnaround time is drastically reduced compared to fully-resolved rotor cases. The results are also promising, with the key features of complex wake-rotor-structure interactions being captured.

In the present work, a time-averaged rotor disk model is applied to NASA's tiltwing UAM concept operating in airplane and helicopter mode. A loose coupling approach ensures an accurate prediction of blade motions and airloads. A comparative study of the physics of this model with blade-resolved rotor simulations (Ref. 12) will be presented to highlight the limitations and efficiencies of each methodology. Performance metrics, airloads, and the rotor wake geometry will be analyzed.

NUMERICAL APPROACH

NASA's OVERFLOW CFD flow solver (Ref. 13) is utilized in this study. OVERFLOW uses high-order accurate finite-difference schemes to solve the Reynolds-Averaged Navier-Stokes equations on a system of structured overset grids. NASA's Chimera Grid Tools (CGT) (Ref. 14) software package is used to generate the overset grids for the rotor disks and the complete vehicle. OVERFLOW has been loosely-coupled with the comprehensive code CAMRAD II (Ref. 15) to account for aircraft trim, and obtain a more accurate and complete model of the vehicle.

Overset Grid Generation

The use of overset grids simplifies the grid generation for complex geometries. Components are broken down into simpler shapes and individual grids are generated for each one. These near-body (NB) grids are attached to the bodies and move with them whereas a collection of stagnant Cartesian off-body (OB) grids cover the surroundings. With CGT, the overset grid generation process may be decomposed into four steps: geometry processing, surface grid generation, volume grid generation, and domain connectivity (Ref. 14).

The geometry is usually obtained from a computer-aided design (CAD) model or a 3D-scanning point cloud. Figures 1a and 1b show the CAD geometry used for the tiltwing vehicle in airplane and helicopter mode. In solid modeling, the boundary representation (BRep) of an object describes its boundaries holding both the topological entities and the geometric components (Ref. 16). A pre-processing step generates discrete surface representations from the analytical BRep solid contained in STEP or IGES files. Access to the model topology and entities is accomplished through EGADS (the Engineering Geometry Aircraft Design System) API which is a foundational component of the Engineering Sketch Pad (Ref. 16). For each body in the geometry, the `egads2srf` tool generates a surface grid file containing a set of structured surface patches on tessellated untrimmed BRep faces. Figures 1c and 1d show the structured untrimmed patches obtained using EGADS for the tiltwing aircraft. A curve grid file is also created that contains structured curves on tessellated BRep edges. Both files are used as inputs in the overset surface grid generation step.

Once the geometry has been processed as reference curve and surface files, structured surface grids are generated using a combination of algebraic and hyperbolic methods. The generation of surface grids is the step that requires the most manual

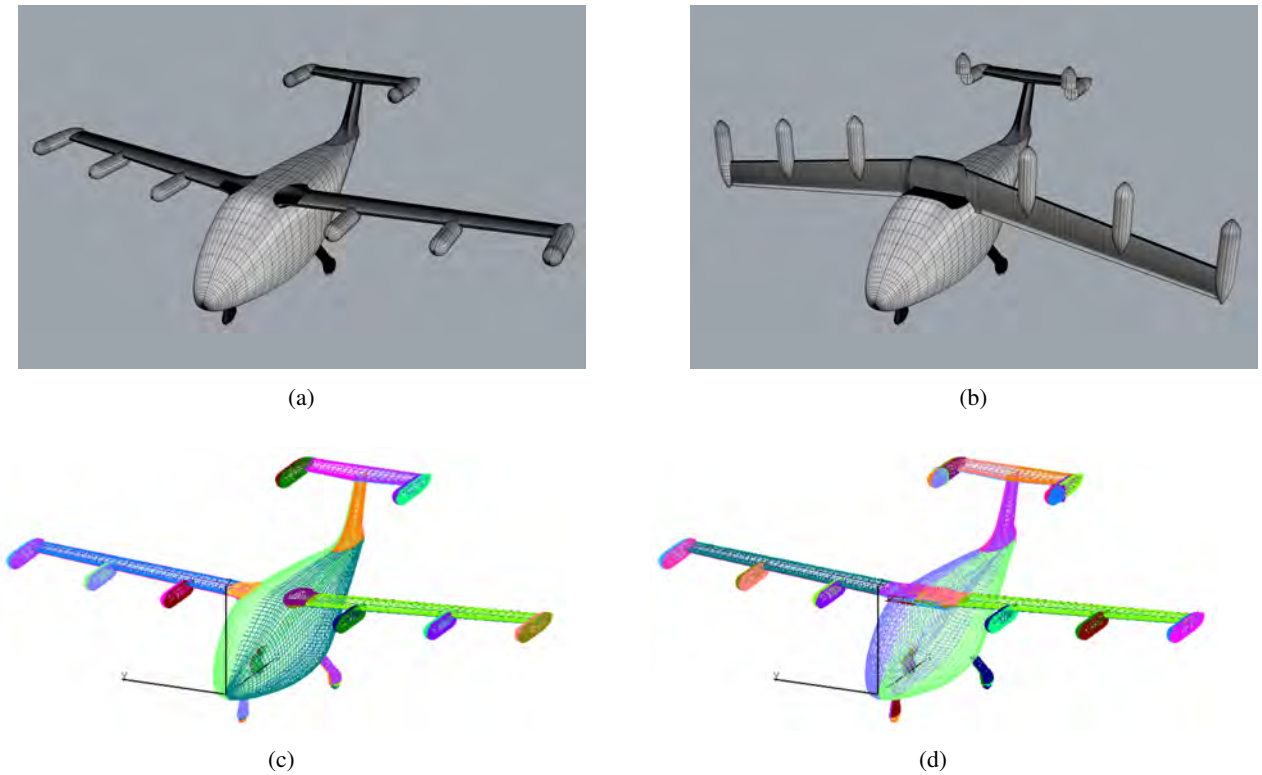

(a) (b)

(c) (d)

Figure 1: The tiltwing vehicle air taxi airframe: (a) CAD geometry for airplane mode and (b) helicopter mode, and structured untrimmed patches obtained with EGADS for (c) airplane mode (d) and helicopter mode. These patches are used as reference surfaces to generate the overset grids.

effort and experience from the user. Figures 2a and 2b show the overset grids for the tiltwing vehicle in airplane and helicopter mode, respectively. The complete vehicle consists of the fuselage, wing, tail, rotor disks, nacelles, and landing gear. The rotor naming convention and spin direction are also indicated. Rotors on the starboard side rotate in a counterclockwise direction whereas rotors on the port side rotate in a clockwise direction.

If surface grids have sufficient overlap, the volume grids are then created using hyperbolic marching methods which extend the grid out to a fixed distance from the surface. Tight clustering in the normal direction near the wall is maintained to achieve good boundary layer resolution in viscous flow computations. The normal grid spacing of all grids at the walls maintains $y^+ \leq 1$. Mesh orthogonality is maximized to provide better solution accuracy. NB volume grids are extended ensuring that the outer boundaries are outside the boundary layer. The NB grids are contained inside the OB Cartesian grids, which extend to the far-field boundary condition located 25 wing semispans away from the vehicle in all directions..

Rotor modeling

The mid-fidelity approach treats the rotor as an infinitely thin disk whereas in the high-fidelity approach, the rotor geometry is meshed. In the former case, the description of the blade geometry is replaced by a cylindrical polar grid containing

Table 1: Tiltwing rotor geometric parameters.

Parameter	Value
Number of blades per rotor	5
Radius R	3.666 ft
Root chord c_{root}	1.252 ft
Tip chord c_{tip}	0.455 ft
Thrust-weighted solidity σ	0.2825

the surface swept by the rotor. Using the *JKL* convention, the rotor plane lies on a constant J plane, with J increasing in the slipstream direction opposite to the thrust vector. K is the periodic direction that wraps around the polar axis with uniform azimuthal spacing. The L index increases along the blade span from the rotor origin to an outer boundary at $r = 1.35R$. The rotor is located between arbitrary L indices that depend on the cutout and tip positions. The grid resolution is clustered near the root, the tip, and the disk plane as shown in figure 3a.

In blade-resolved simulations, overset moving grids are generated for the blades from the information gathered in table 1. The profiles used to build the blade are 10.6 % thick modern airfoils from $r = 0$ to $r = 0.85R$, and 9 % thick modern airfoils from $r = 0.95R$ to the tip $r = R$. The root cutout is $r = 0.2R$. The transition between the two different airfoil sections is smooth —linear interpolation with the radial stations. The blade has a taper of $4/11$. The blade grids are shown in

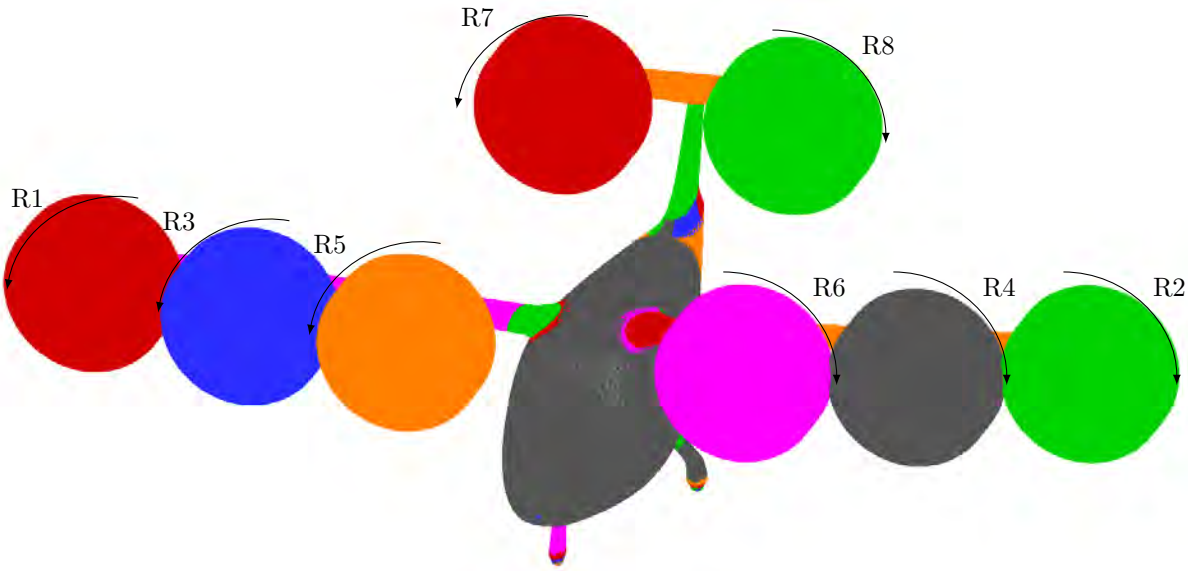

(a)

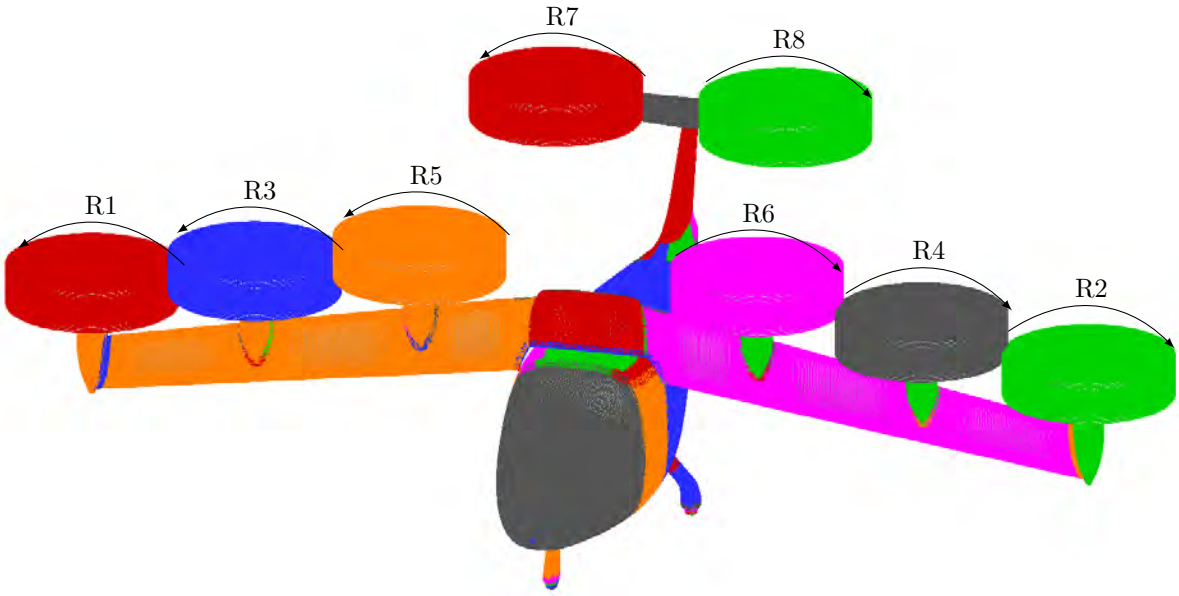

(b)

Figure 2: Tiltwing overset surface grids for the complete vehicle in (a) airplane mode and (b) helicopter mode. The complete vehicle consists of eight rotor disks, fuselage, wing, tail, nacelles, and landing gear.

detail in figure 3b. The surface grid resolution is clustered in the chordwise direction near the airfoils' leading and trailing edges, regions characterized by large pressure gradients. By the same token, the spanwise direction is clustered near the blades' root and tip.

High-Order Accurate Navier-Stokes Solver

The Navier-Stokes equations can be solved using finite differences with a variety of numerical algorithms and turbulence models. The unsteady Reynolds-Averaged Navier-Stokes (RANS) equations are solved in strong conservation form:

$$\frac{\partial \vec{q}}{\partial t} + \frac{\partial (\vec{F} - \vec{F}_v)}{\partial x} + \frac{\partial (\vec{G} - \vec{G}_v)}{\partial y} + \frac{\partial (\vec{H} - \vec{H}_v)}{\partial z} = 0, \quad (1)$$

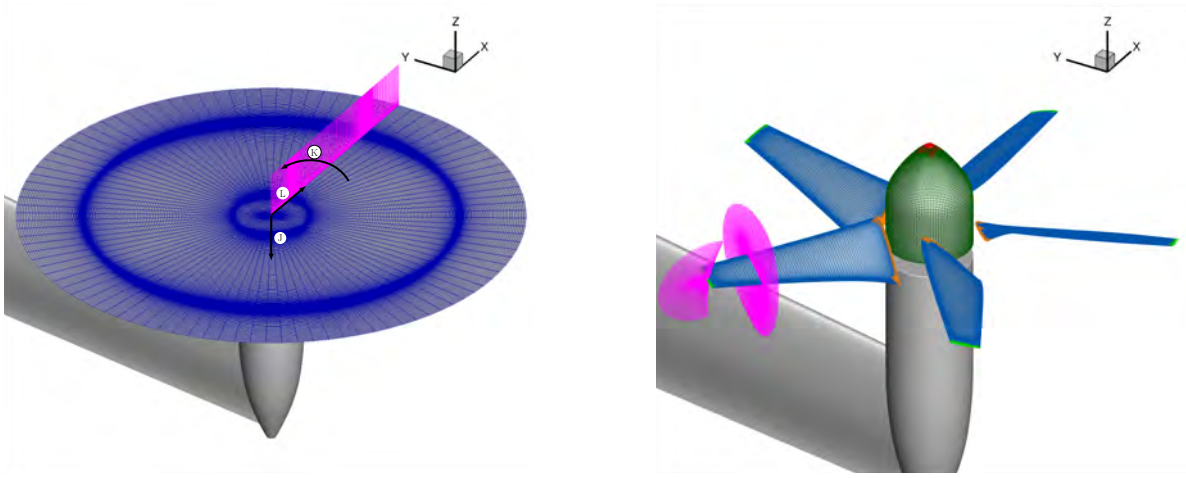

(a) (b)

Figure 3: Blade grids for the tiltwing vehicle: (a) cylindrical polar grids for rotor disk simulations and (b) overset moving grids for blade-resolved simulations. Slices of volume grids are colored in magenta.

being $\vec{q} = [\rho, \rho u, \rho v, \rho w, e]^\intercal$ the vector of conserved variables; $\vec{F}$, $\vec{G}$ and $\vec{H}$ the inviscid flux vectors; and $\vec{F}_\mathrm{v}$, $\vec{G}_\mathrm{v}$ and $\vec{H}_\mathrm{v}$ the viscous flux vectors.

In the numerical model of the rotor disk, the RANS equations are solved using an HLLE++ upwind scheme (Ref. 17) with the 5$^{\text{th}}$-order accurate spatial option. The flow field around the blades is replaced by spatially- and time-averaged loads acting on the flow. To that end, source terms (Ref. 11) are added to the right-hand side of equation 1 for the cells in which the rotor is located:

$$\vec{S} = \left[0, f_x, f_y, f_z, \vec{f} \cdot \vec{v}\right]^\intercal, \tag{2}$$

where $\vec{f}$ is the local force per unit area for the disk, able to vary with the radial and azimuthal positions. These aerodynamic forces are determined from airfoil measured lift, drag, and moment coefficients stored as C81 formatted tables. The local angle of attack and Mach number for each blade section are updated at each time step of the simulation considering the most recently computed RANS solution.

For blade-resolved simulations, the diagonal central difference algorithm is used with the 5$^{\text{th}}$-order accurate spatial differencing option and scalar dissipation. The physical time step corresponds to 0.25° rotor rotation, together with up to 50 dual-time sub-iterations to achieve a 2.5 to 3.0 orders of magnitude drop in sub-iteration residual.

Hybrid Turbulence Modeling

The OVERFLOW code currently includes algebraic, one-equation, and two-equation turbulence models, including the choice of hybrid Reynolds-Averaged Navier-Stokes / Large Eddy Simulation (RANS/LES) models that close the RANS equations. In this study, the one equation Spalart-Allmaras (Ref. 18) turbulence model is used primarily within the boundary layer.

The Detached Eddy Simulation (DES) (Ref. 18) approach provides a good compromise between accuracy and computational cost. The intent of this model is to combine efficiently the best aspects of RANS and LES methodologies in a single solution. Near-wall regions are treated in RANS mode since turbulent scales can be very small and need to be modeled; and the rest of the flow is treated in LES mode, where the largest turbulent scales are grid-resolved. In this way, DES is a RANS/LES hybrid approach that mitigates the problem of artificially large eddy viscosity. The turbulence length scale d is replaced by $\bar{d}$:

$$\bar{d} = \min(d, C_{\mathrm{DES}}\Delta), \tag{3}$$

which is the minimum of the distance from the wall d and C_{DES} times the local grid spacing Δ.

The DES approach assumes that the wall-parallel grid spacing $\Delta_{||}$ exceeds the thickness of the boundary layer δ so that the RANS model remains active near solid surfaces. If the wall-parallel grid spacing is smaller than the boundary layer thickness $\Delta_{||} < \delta$, then the DES Reynolds stresses can become under-resolved within the boundary layer; this may lead to non-physical results, including grid-induced separation. Using Delayed Detached Eddy Simulation (DDES) (Ref. 19), the RANS mode is prolonged and is fully active within the boundary layer. The wall-parallel grid spacing used in this study does not violate the hybrid-LES validity condition; thus, DES and DDES should give similar results. Nevertheless, all computations have been performed using the DDES formulation for both NB and OB grids.

Comprehensive Analysis

Structural dynamics and rotor trim for the coupled calculations are performed using the comprehensive rotorcraft analysis code CAMRAD II (Ref. 15). CAMRAD II is a software code for the aeromechanics analysis of rotorcraft that incorporates a combination of advanced technologies, including multibody dynamics, nonlinear finite elements, and rotorcraft aerodynamics.

The trim task finds the equilibrium solution for a steady-state operating condition and produces the solution for performance, loads, and vibration. The aerodynamic model for the rotor blade is based on lifting-line theory, using two-dimensional airfoil characteristics and a vortex wake model. CAMRAD II has undergone extensive correlation with performance and load measurements on rotorcraft.

Loose Coupling OVERFLOW - CAMRAD II

The coupling procedure introduced by Potsdam et al. (Ref. 20) is applicable to blade-resolved simulations and involves the exchange of integrated section aerodynamic loads and blade sectional motions at the quarter-chord. For the rotor disk option (Ref. 11), the motion interface is modified to account for the blade motions through control angles instead of quarter-chord displacement data. Figure 4 summarizes the loose coupling approach.

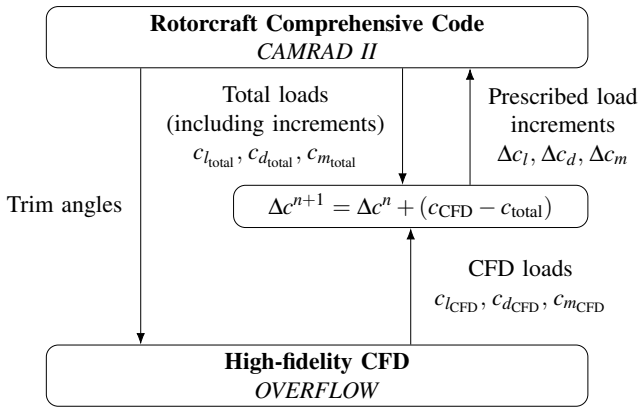

Figure 4: Flow diagram for CFD/CSD loose coupling methodology for rotor disk simulations.

The simulation is initialized with a comprehensive analysis resulting in a trimmed rotor solution obtained with lifting line aerodynamics. As part of the trim solution, CAMRAD II calculates the control angles, which are given to the CFD. The CFD analysis accounts for the entire flow field. The source terms are unknown at the start of the simulation and evolve as part of the solution. The CFD is run with the prescribed angles and provides the flow field relative to the blade sections located at the rotor disk plane. Knowing the angle of attack and Mach number, local aerodynamic coefficients are retrieved from C81 airfoil tables. Then, the source terms are added to the governing equations of the computational cells lying on the rotor blade path as external forces acting on the fluid. OVERFLOW outputs the normal force N', pitching moment M', and chord force C' as a function of radius and azimuth. Then, the aerodynamic force and moment coefficient increments Δc that are used in the comprehensive code at the next iteration $n+1$ are calculated. The increments are the difference between the CFD loads and the comprehensive lifting line solution required to trim from the previous step n, plus the load increments from the previous step:

$$\Delta c^{n+1} = \Delta c^n + (c_{\text{CFD}} - c_{\text{total}}). \tag{4}$$

For the initial step, the increments are the difference between CFD and the total loads from the 0^{th} run in CAMRAD II:

$$\Delta c^1 = c_{\text{CFD}} - c_{\text{total}}. \tag{5}$$

The sectional pitching moment $M^2 c_{\text{m}}$, normal force $M^2 c_{\text{n}}$, and chord force $M^2 c_{\text{c}}$ coefficients are defined as:

$$M^2 c_{\text{m}} = \frac{M'}{\frac{1}{2}\rho a^2 c^2}, \tag{6}$$

$$M^2 c_{\text{n}} = \frac{N'}{\frac{1}{2}\rho a^2 c}, \tag{7}$$

$$M^2 c_{\text{c}} = \frac{C'}{\frac{1}{2}\rho a^2 c}. \tag{8}$$

The trim update provides the new control angles of the re-trimmed rotor. Then, the CFD is rerun using the previous flow solution as a restart condition. Periodicity requirements for the coupling only apply to time-accurate calculations, when there is an equivalence between the physical time step and rotor rotation. For the disk model, the coupling can be done at any arbitrary number of time steps. In this work, the solution is coupled every 1000 flow solution steps in OVERFLOW, which showed improved convergence over coupling every 2000 or 3000 steps. Convergence is achieved when collective and cyclic control angles and the CFD aerodynamic forces do not change between iterations within a small tolerance.

RESULTS

NASA's tiltwing UAM concept has been simulated in airplane and helicopter mode using the high-fidelity CFD flow solver OVERFLOW and the rotorcraft comprehensive code CAMRAD II. The simulation process involves an iterative exchange of information, with CAMRAD II providing OVERFLOW with a trimmed flight solution in the form of control angles for the rotor disk approximation, or a set of rigid blade motions for the blade-resolved simulations. OVERFLOW then solves the time-dependent Navier-Stokes equations and returns a correction of the airloads to CAMRAD II. When the coupling approach is converged, the CFD solution replaces the comprehensive code aerodynamics. The simulations have been run using NASA's supercomputers Pleiades, Electra, and Aitken located at the NASA Advanced Supercomputing (NAS) Division.

In the absence of experimental data, the reference used for the present study is the high-fidelity solution from Garcia Perez et al. (Ref. 12). The previous work identified certain areas of improvement in the trim coupling procedure. Achieving a correct trim solution for the tiltwing vehicle requires updating the pitch angle of the aircraft, modeling the control surfaces on the wing and tail, and exchanging integral loads on every component between the CFD solver and the comprehensive code. To ensure a fair comparison, the same geometry and trim simplifications were employed. Namely, the trim procedure is applied to the rotors only, all control surfaces remain

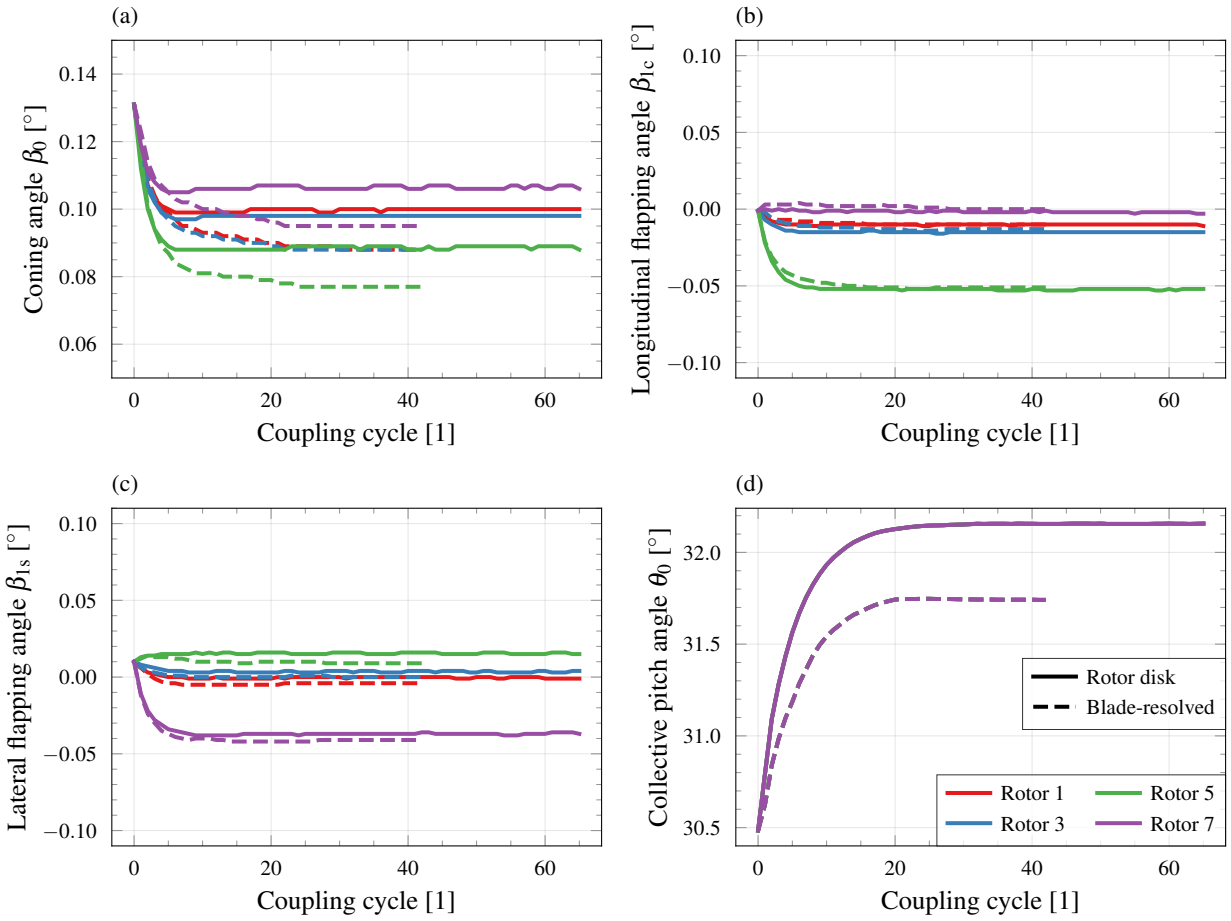

Figure 5: Convergence history of the rotor trim angles in airplane mode: (a) coning angle β_0, (b) longitudinal flapping angle β_{1s}, (c) lateral flapping angle β_{1c}, and (d) collective pitch angle θ_0.

undeflected, and the vehicle incidence angle is also kept at zero.

In the sections that follow, an analysis of the trim solution, wake geometry, and rotor performance will be presented for each flight condition. This analysis will focus on the differences observed for each methodology. Due to symmetry and for clarity purposes, plots will only include rotors located on the starboard side.

Airplane mode

The simulations in cruise are conducted in a standard atmosphere at an altitude of $h = 6000\,\text{ft}$. The freestream velocity is $V_\infty = 145\,\text{kt}$ and the propellers tip speed is set to $V_{\text{tip}} = 300\,\text{ft/s}$. This results in a reference Mach number of $M = 0.274$ and a Reynolds number based on the mean chord of $Re = 1.65 \times 10^6$.

Table 2 summarizes the total number of grid points, the number of processors utilized, and the turnaround time required for each model. Since the rotor geometry is no longer present, the rotor disk simulation reduced the total number of grid points by more than 50 %; and it was completed in 72 wall-clock hours with 1200 processors. In contrast, the blade-resolved simulation finished in 600 wall-clock hours utilizing 2400 processors. In summary, the rotor disk approximation reduces the turnaround time by 88 % and utilizes half of the computational resources.

Table 2: Grid points, number of processors, and wall-clock time for airplane mode simulations.

	Rotor disk	Blade-resolved
Total grid points	185×10^6	421×10^6
Number of processors	1200	2400
Wall-clock time	72 h	600 h

Trim solution The coupling approach is considered converged when the comprehensive code airloads equal the CFD airloads, and the control angles and delta-airloads remain unchanged with the iteration number.

Figure 5 shows the convergence history of the rotor flapping angles and collective pitch. The coning angle β_0 is the result of the balance between inertial and aerodynamic forces acting on the rotor blades. The same CAMRAD II input decks, which

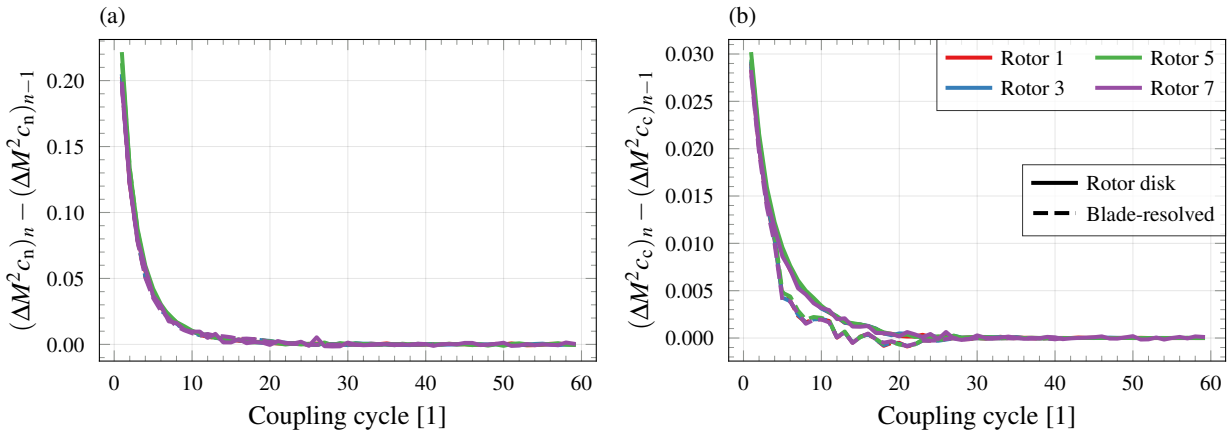

Figure 6: Convergence history of the delta-airloads approach in airplane mode represented as the change between iterations for the (a) sectional normal force coefficient $M^2 c_n$ and (b) chord force coefficient $M^2 c_c$. The results are expressed in airfoil axes.

Table 3: Converged thrust and torque coefficients for the rotors in airplane mode as predicted by rotor disk and blade-resolved simulations.

	Rotor disk		Blade-resolved		Percentage change	
	$C_T \times 10^3$ [1]	$C_Q \times 10^3$ [1]	$C_T \times 10^3$ [1]	$C_Q \times 10^3$ [1]	Thrust [%]	Torque [%]
Rotor 1	9.432	10.190	9.118	10.470	3.44	−2.66
Rotor 2	9.407	−10.170	9.118	−10.470	3.17	−2.84
Rotor 3	9.138	9.961	9.021	10.370	1.30	−3.93
Rotor 4	9.139	−9.960	9.021	−10.370	1.31	−3.93
Rotor 5	7.319	8.376	7.009	8.592	4.42	−2.52
Rotor 6	7.322	−8.377	7.010	−8.592	4.45	−2.50
Rotor 7	10.960	11.270	10.530	11.490	4.14	−1.91
Rotor 8	10.940	−11.250	10.520	−11.480	4.01	−2.00

contain information about the mass and inertia model, were used in both approaches. Hence, the differences in β_0 will be determined purely by the aerodynamic forces, that is to say, higher thrust results in a higher coning angle. The agreement for the longitudinal β_{1c} and lateral β_{1s} flapping angles is very good. As for the collective pitch θ_0, the evolution is similar for all rotors, with the disk model predicting values approximately 2° higher. After about 23 coupling iterations, the control angles reached a converged solution. Generally, the flow solution needs to be run longer for the wake to develop and for the forces and moments on other components located within the wake to converge.

Figure 6 illustrates the delta-coupling convergence history to verify that the corrected aerodynamic loads calculated by the comprehensive code approach the CFD airloads. As mentioned, the convergence is determined by ensuring that the delta-airloads remain constant between iterations —see equation 4. This condition is satisfied after 30 coupling cycles.

Table 3 displays the final thrust C_T and torque C_Q coefficients obtained. The results are divided into three columns: "Rotor disk", which shows the mid-fidelity solution; "Blade-resolved", which shows the high-fidelity solution; and "Percentage change", which indicates the relative change of the rotor-disk computed airloads in comparison to the blade-resolved solution and is expressed as a percentage. In the case of the blade-resolved simulation, the results reflect the flow average solution over the last rotor revolution, or 1440 time steps. Since there is no direct equivalence between the pseudo-time step number and the rotor revolutions for the rotor disk simulation, the results have been calculated as running averages with a window of 5000 pseudo-time steps.

Rotors in symmetric positions generate equal thrust and apply opposing torques to the airframe, effectively canceling out yawing and rolling moment contributions. The aerodynamic interactions between the rotors and the airframe vary depending on the placement of the rotors. For wing rotors, those closer to the fuselage produce less net thrust. For example, the thrust coefficient of rotors 5-6 decreases by 20 % compared to rotors 1-2. Rotors 7-8 generate the highest amount of thrust. The torque coefficients exhibit similar trends. The disk model overpredicts the thrust coefficient and underpredicts the torque coefficient. For the former coefficient, the largest differences occur at slightly below 5 % for rotors 5-6. For the latter, the largest differences are below 4 % for rotors 3-4.

In order to investigate the blade loading distribution, contour maps of the sectional normal force coefficient $M^2 c_n$ and chord

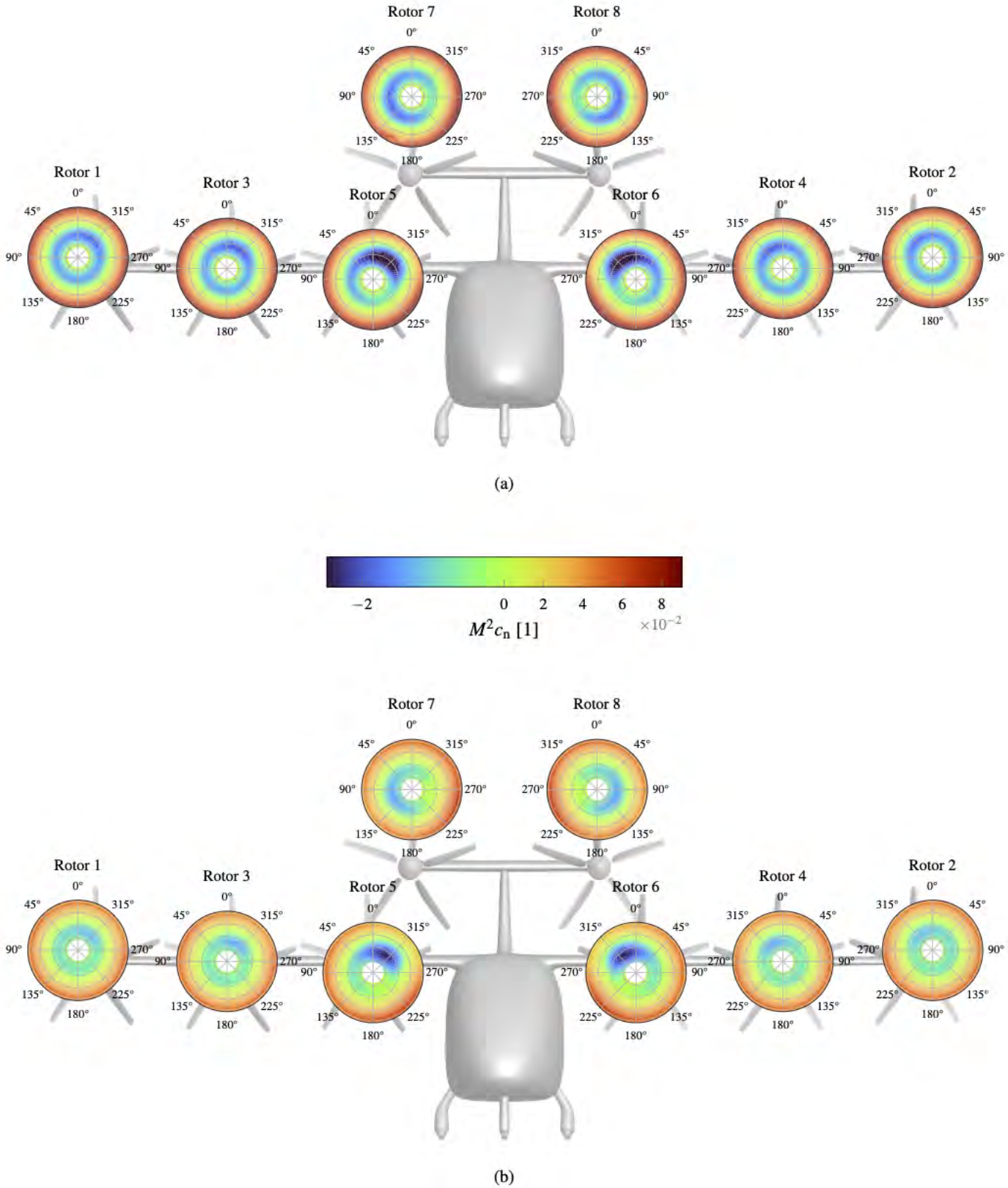

Figure 7: Sectional normal force coefficient M^2c_n distribution in airplane mode: (a) rotor disk and (b) blade-resolved simulations.

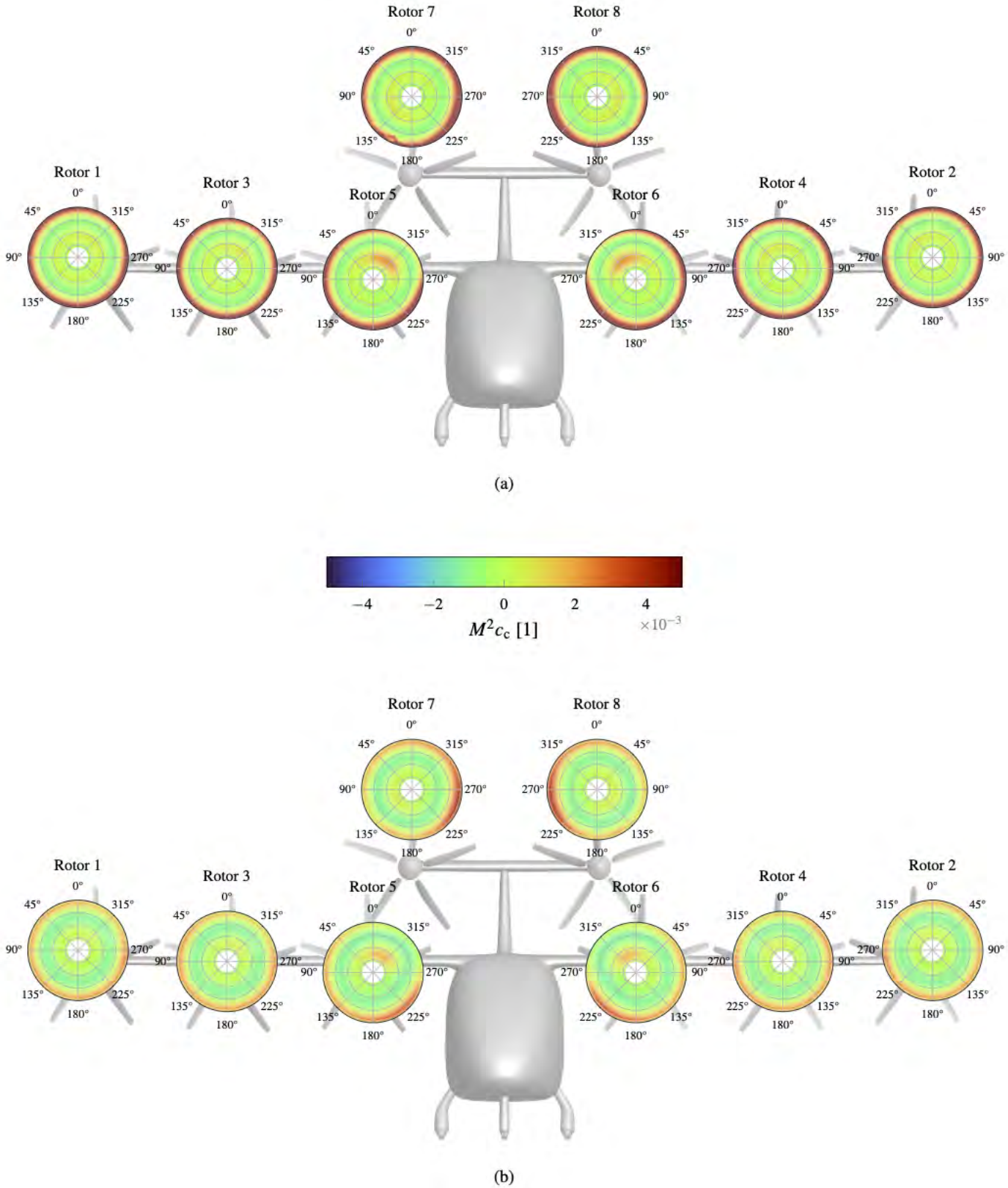

Figure 8: Sectional chord force coefficient $M^2 c_c$ distribution in airplane mode: (a) rotor disk and (b) blade-resolved simulations.

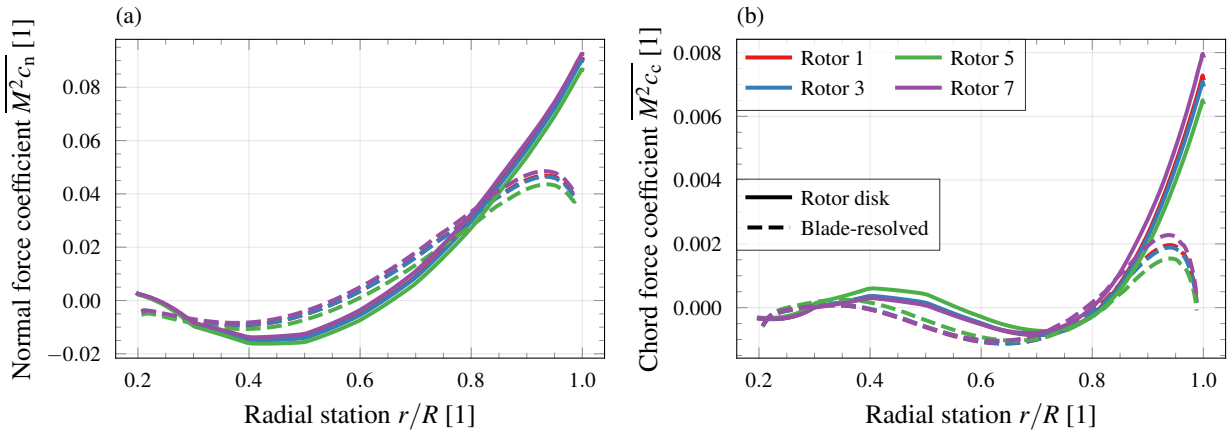

Figure 9: Evolution of mean sectional airloads with the radial station in airplane mode: (a) normal force coefficient $M^2 c_n$ and (b) chord force coefficient $M^2 c_c$. The results are expressed in airfoil axes.

force coefficient $M^2 c_c$ are shown in figures 7 and 8, respectively. The azimuth angle ψ is measured in hub axes, positive in the direction of rotation, and divides the rotor area into four quadrants of $\psi = 90°$ each. The coefficients are nondimensionalized by the speed of sound. Each figure shows a front view image of the vehicle with the rotor maps obtained from rotor disk and blade-resolved simulations.

The normal force distribution increases towards the tip due to a higher dynamic pressure. The most notable feature in figure 7 is the appearance of areas of negative thrust that extend from the root up to radial positions $r = 0.6R$. In those areas, the local angle of attack α seen by the blades is negative. From the blade element theory, the angle of attack is given by:

$$\alpha = \theta - \phi = \theta - \arctan \frac{V_\infty + v_i}{\Omega r}. \tag{9}$$

Equation 9 has two addends: the pitch angle θ and the inflow angle ϕ. The pitch angle is the sum of the collective pitch and geometric twist, since no cyclic controls were applied. The inflow angle is determined by the components of the local velocity vector: the normal velocity consists of the freestream velocity V_∞ and the induced velocity v_i; the in-plane velocity is due to the rotation of the blades at rate Ω. The inflow angle is large across the entire rotor disk due to the freestream velocity. This is aggravated in sections near the root, where the in-plane velocity is low. The angle of attack becomes negative in these sections thus the thrust is negative. If the rotors were operating in isolation, this condition would affect the rotors axisymmetrically. However, complex rotor-wake-airframe aerodynamic interactions introduce disturbances to the inflow that modify the extent and location of those areas. The airframe affects primarily rotors 5-6. For those, no-thrust areas extend over the first and especially fourth quadrants. Additionally, the tip of the blade sees increased loading towards the tip in the third quadrant, when the blades are moving upwards next to the fuselage. The influence of the fuselage is less pronounced for wing rotors located further away, for which the normal force distribution looks axisymmetric. Rotors 7-8 spin in opposite directions close to each other, which increases the tip loading in the third and fourth quadrants.

The sectional chord force coefficient distribution, plotted in figure 8, also reflects an increase in asymmetry for rotors placed closer to the fuselage. In the blade-resolved solution, we observe discontinuities for rotors 1-2 and 3-4 in the transition from the third to fourth quadrant. These are thought to be due to interactions with the wake of the neighboring rotor, which is also slightly upstream, as the ascending blade encounters a descending tip vortex. The rotor disk solution, however, is not able to capture these interactions since the tip vortex is not resolved. The peaks of the force coefficient are located at the same azimuthal positions as in the normal force contour map: the third quadrant for rotors 5-6, and the third and fourth quadrants for rotors 7-8.

Overall, the agreement between blade-resolved and rotor disk simulations is satisfactory, with the latter overpredicting the results near the tip. To further study this behavior, the forces have been plotted per nondimensional unit span in figure 9. For sections up to $r = 0.85R$, the agreement between rotor disk and blade-resolved is good. For sections beyond $r = 0.9R$, the airloads are significantly overestimated, by a factor of two for the normal force and by a factor of four for the chord force. Because of its intrinsic two-dimensional nature, the blade element theory (BET) approximation used in the rotor disk model breaks near the tip, leading to nonzero loading. Usually, BET is supplemented with tip correction models to account for this phenomenon. In this preliminary study, tip correction models were not considered and their influence is left for future work.

In a trimmed horizontal flight, the sum of the forces and moments about the center of gravity (CG) are balanced. The longitudinal trim in CAMRAD II considers the horizontal force F_x, the vertical force F_z, and the pitching moment M_y in airframe axes. Figures 10, 11, and 12 show the breakdown of these forces and moment acting on different parts of the vehicle. The top plot shows the evolution as the solution progresses in time or pseudo-time. In the blade-resolved simulation, the loads

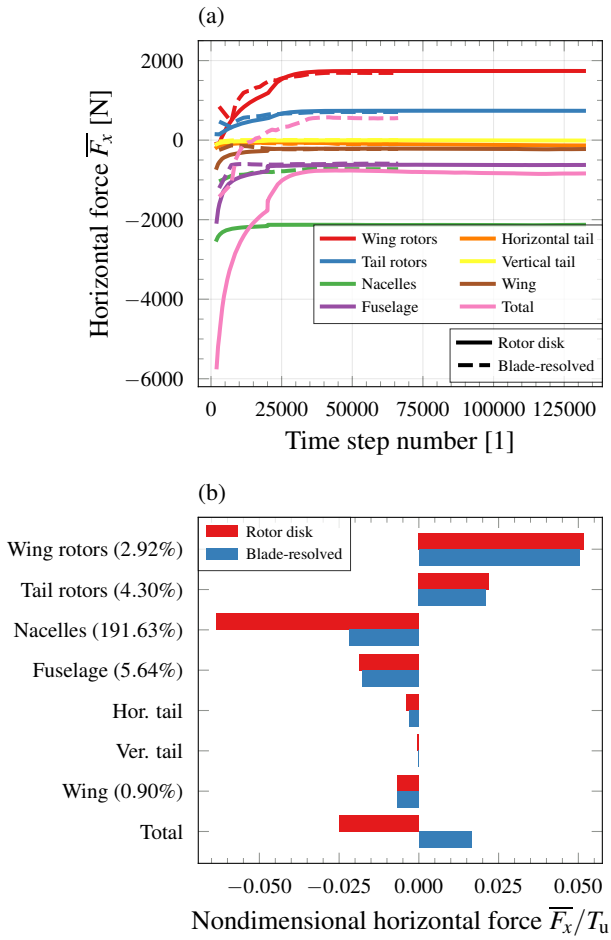

Figure 10: Trim solution for the aerodynamic forces in the horizontal direction in airplane mode: (a) evolution with the time/pseudo-time step number; (b) converged solution and percentage change.

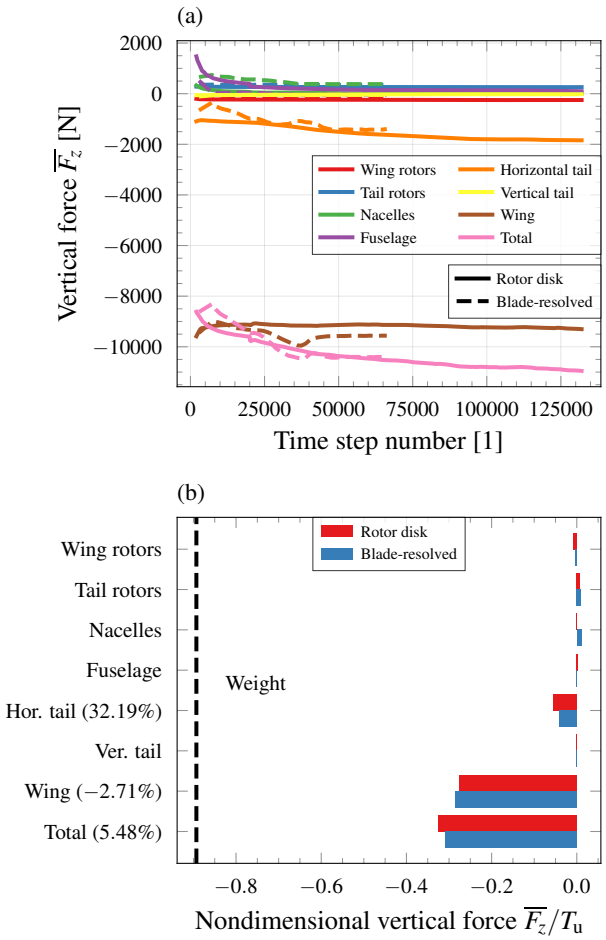

Figure 11: Trim solution for the aerodynamic forces in the vertical direction in airplane mode: (a) evolution with the time/pseudo-time step number; (b) converged solution and percentage change.

are averaged over 1440 time steps, or one rotor revolution; in the rotor disk simulation, the loads are averaged taking sliding windows of 5000 pseudo-time step numbers. The bottom plot shows a side-by-side comparison of the converged values obtained from both models. These have been nondimensionalized by characteristic magnitudes of thrust T_u and torque Q_u defined from the tip speed:

$$T_u = \rho A(\Omega R)^2, \qquad Q_u = \rho AR(\Omega R)^2. \tag{10}$$

The percentage change relative to the blade-resolved solution is indicated in parentheses. Note that if the reference value is close to zero, or if the two values have opposite signs, the relative change is not well defined. This happens for the vertical and horizontal sections of the tail. For these cases, the metric has been omitted. Additionally, it has also been omitted for components that account for less than 3 % of the total force/moment contribution, as the result is within trim tolerance.

Figure 10 summarizes the trim solution of the horizontal force F_x. In airplane mode, the rotors act as propulsive devices, balancing the drag generated mainly by the nacelles, fuselage —which includes the landing gear—, wing, and to a lesser degree, horizontal tail. In accordance with table 3, the rotor disk value for wing and tail rotors is within 5 % of the blade-resolved value. Good agreement is also observed for the fuselage (5.64 %) and the wing (0.89 %), indicating that the disk model is able to predict the rotor installation effects on other components. The most notable difference is observed for the nacelles (191.61 %). This can be explained by examining the wake structure in figure 13. For the disk model, the rotating part of the nacelle, or spinner, was removed. The oncoming flow encounters a blunt body in the vicinity of the flat-faced static part of the nacelle, coming almost to rest and increasing the pressure. The flow then separates, generating an area of low pressure downstream. In the blade-resolved simulation, the high pressure is localized in a smaller area on the spinner, and the flow remains attached to the nacelle. As a result, the pressure drag is significantly smaller than that predicted by the disk model. Lastly, it is worth noting that the total horizontal force trims to nonzero values. This is one of the limitations of the current loose coupling approach, which involves only the ex-

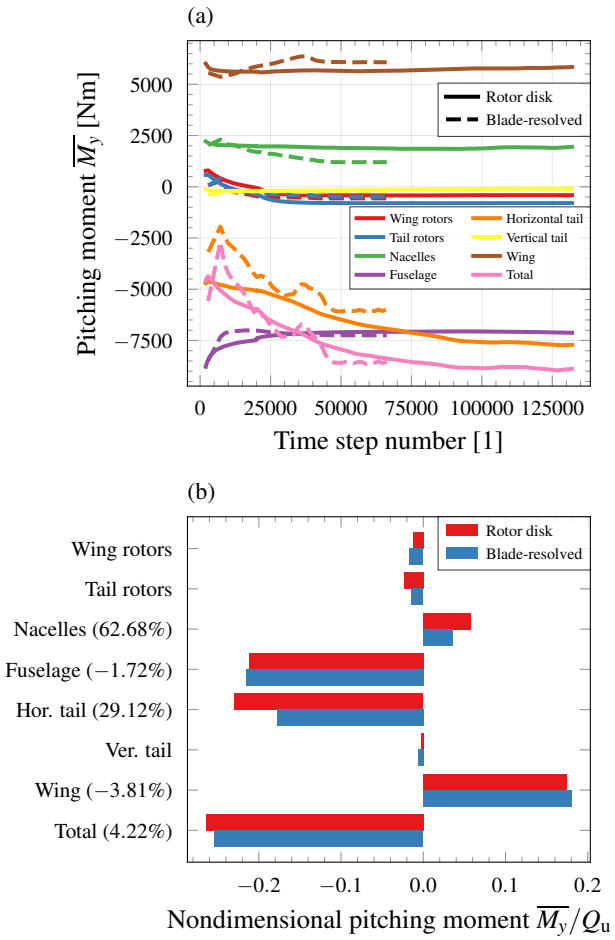

Figure 12: Trim solution for the pitching moment about the center of gravity in airplane mode: (a) evolution with the time/pseudo-time step number; (b) converged solution and percentage change.

change of rotor loads at the interface OVERFLOW/CAMRAD II. Without correction from the CFD solution, the comprehensive code aerodynamic models for the fuselage, wing, and tail are still active for the trim task. Efforts in the future will be directed toward adding that capability for more accurate calculations.

The trim solution for the aerodynamic forces along the z-axis is shown in figure 11. Lift is generated mainly by the wing and horizontal tail. Errors in the lift prediction are larger for the horizontal tail (32.17 %) than the wing (2.71 %), but its contribution to the total is not as important. The forces plotted correspond to the CFD solution, which receives a trim update only for the rotor loads. Additionally, the pitch angle of the vehicle is fixed to zero, and that effectively imposes a constraint on the wing angle of attack, limiting the amount of lift generated. The aerodynamics of the other components belongs in the comprehensive analysis part of the iteration. This explains why the vertical aerodynamic force is unable to compensate the vehicle's weight, marked in the plot by a dashed vertical line.

Finally, figure 12 illustrates the trim solution of the pitching moment M_y about the center of gravity. Components involved in the moment balance are the fuselage, wing, horizontal tail, and nacelles. The fuselage and horizontal tail produce a nose-down moment whereas the wing and the nacelles produce a nose-up moment. The agreement on moment prediction is good for the fuselage (1.73 %) and for the wing (3.81 %). Larger differences are observed for the nacelles (62.7 %) and the horizontal tail (29.10 %). In such cases, the large errors observed in the forces —horizontal force for the nacelles and vertical force for the horizontal tail— will translate to the pitching moment. These errors have a canceling effect on the total difference observed (4.21 %) since the moments oppose each other. Control surfaces are required for trimming the vehicle. In particular, the elevator would allow to control the attitude, balancing the pitching moment about the CG.

Wake geometry The wake geometry is visualized through the representation of iso-surfaces of Q-criterion shaded by vorticity magnitude. Figure 13 shows a perspective front view of the vortex wake for rotor disk and blade-resolved simulations. The amount of details of the wake structure captured by each approach is clearly different.

On the one hand, the mid-fidelity simulation portrays a time- and space-averaged rotor solution. Since the loading is distributed across the entire rotor disk, vorticity is concentrated in a vortex sheet at the tip. This vortex sheet outlines the edge of the modeled rotor. Flow separation is observed at the nacelles. Without the spinners, the freestream encounters the circular flat face of the nacelle and separates from the surface. This creates a low-pressure region downstream. In addition, the flow creates an almost uniform high-pressure distribution at the circular cross-section of the nacelle, thus increasing the form drag —see figure 10. The detached flow hides the wingtip vortex. Separated flow is also observed from the fuselage, vertical tail, and landing gear.

On the other hand, high-fidelity simulation offers a more accurate and detailed description of the flow field. The most notable difference is the representation of the tip vortices and their interactions with other components. Tip vortex structures shed from the blades describe helical trajectories downstream of the rotors. A similar root-vortex structure can be seen followed by its disintegration. A rapid convection by the freestream reduces BVIs with neighboring blades. The wake of rotors 5-6 is swept toward the fuselage and impinges on rotors 7-8 in the azimuthal range $90° < \psi < 180°$. Rotor positioning on the wing aims to blow the span uniformly and supposedly minimize flow separation during transition maneuvers from helicopter to airplane mode and vice versa. Unlike in the rotor disk simulation, flow is only partially separated behind the inboard and middle nacelles. With the spinners, the nacelles are a streamlined body with a pointy front end that gradually widens. This shape allows the flow to remain attached to the surface. In this case, the wingtip vortices are visible. The spin direction of the rotors is chosen to reduce their strength and improve cruise performance. Lastly, the flow separates from the fuselage, vertical tail, and landing gear.

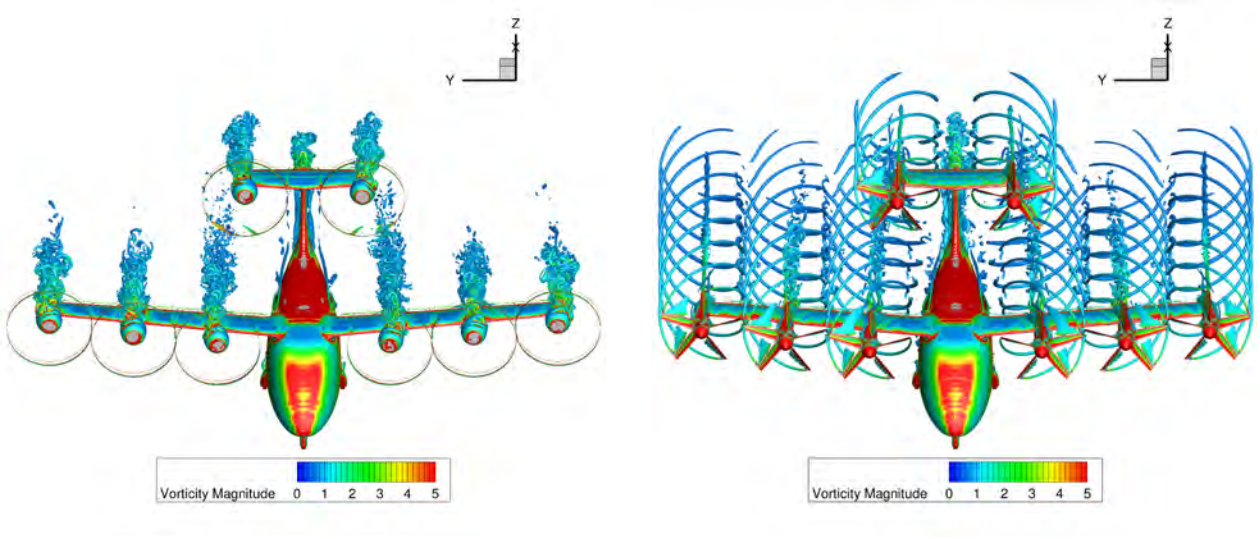

(a) (b)

Figure 13: Snapshot in time of the iso-surfaces of Q-criterion shaded with the vorticity magnitude in airplane mode: (a) rotor disk and (b) blade-resolved simulations.

Performance The performance of the cruise operation is measured in terms of propulsive efficiency η, which is the ratio of propulsive power to input power:

$$\eta = \frac{TV_\infty}{P}, \tag{11}$$

with T being the rotor thrust, V_∞ the freestream velocity, and P the input power.

The propulsive efficiencies were obtained with three approaches of varying fidelity, from high to low: blade-resolved and rotor disk simulations coupling OVERFLOW/CAMRAD II, and CAMRAD II free wake, as shown in table 4. Overall, the results of the mid- and low-fidelity models show reasonable agreement. For CAMRAD II free wake, the largest percentage difference is found in the performance prediction of rotors 5-6, with almost a 10 % difference.

Table 4: Rotor performance in airplane mode measured by the propulsive efficiency. The results are obtained using: OVERFLOW blade-resolved simulations, OVERFLOW rotor disk modeling, and CAMRAD II free wake.

	Propulsive efficiency η		
	OVERFLOW/CAMRAD II		CAMRAD II
	Blade-resolved	Rotor disk	Free wake
Rotor 1	0.6978	0.6917	0.7149
Rotor 2	0.6982	0.6932	0.7149
Rotor 3	0.6973	0.6874	0.7113
Rotor 4	0.6971	0.6886	0.7113
Rotor 5	0.6460	0.6578	0.7086
Rotor 6	0.6461	0.6578	0.7086
Rotor 7	0.7385	0.7307	0.7138
Rotor 8	0.7377	0.7304	0.7138

Differences in other rotors range from 2-4 %. This approach is not able to capture the aerodynamic interactions between the fuselage and the rotors that degrade their performance. For the disk model, the differences are below 2 % even for inboard rotors.

Helicopter mode

The simulations in hover are conducted in a standard atmosphere at an altitude of $h = 6000$ ft. The tip speed of the propellers is $V_{tip} = 550$ ft/s. The reference Mach number is $M = 0.5$ and the Reynolds number based on the mean chord is $Re = 3 \times 10^6$.

Table 5 gathers the total number of grid points, the number of processors used, and the turnaround time for each model. The rotor disk simulation used 1200 processors and required 96 wall-clock hours. The blade-resolved simulation finished in 600 wall-clock hours utilizing 2400 processors. This implies a reduction of 83 % in computational time.

Table 5: Grid points, number of processors, and wall-clock time for helicopter mode simulations.

	Rotor disk	Blade-resolved
Total grid points	184×10^6	417×10^6
Number of processors	1200	2400
Wall-clock time	96 h	600 h

Trim solution Hover is a self-induced low-speed condition with no freestream velocity. Rotor wakes have a long-term influence on rotor aerodynamics, worsening the convergence. Indeed, for the same number of pseudo-time steps, the turnaround time increased by 30 % compared to airplane mode —see tables 2 and 5. Figure 14 shows the convergence history of the

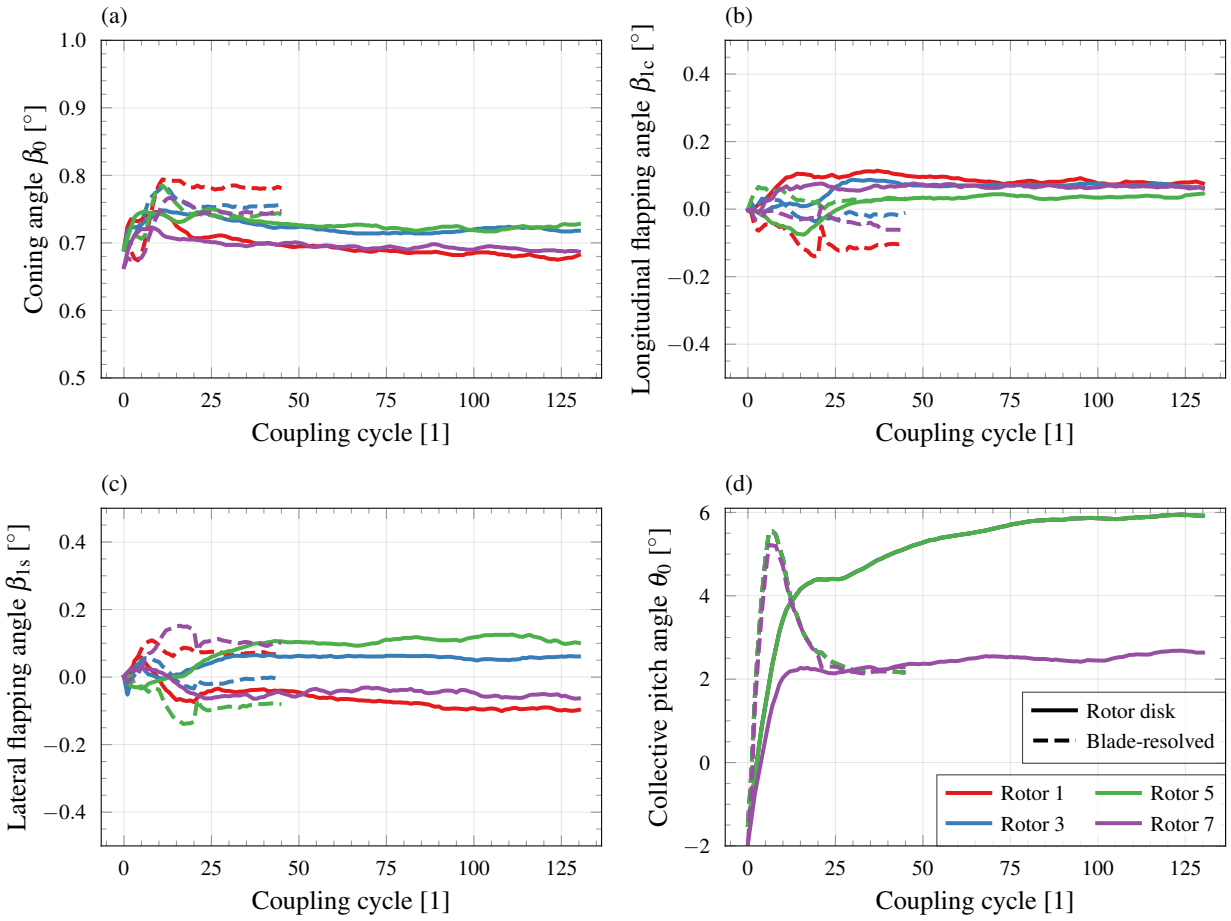

Figure 14: Convergence history of the rotor trim angles in helicopter mode: (a) coning angle β_0, (b) longitudinal flapping angle β_{1s}, (c) lateral flapping angle β_{1c}, and (d) collective pitch angle θ_0.

coning angle β_0, longitudinal flapping angle β_{1c}, lateral flapping angle β_{1s}, and collective pitch angle θ_0. The number of coupling cycles until convergence doubled with respect to the airplane mode condition. The flapping angles stabilize at low levels, with smaller than 0.2° differences observed between rotor disk and blade-resolved cases. In the blade-resolved simulation, the collective pitch angle evolves in the same fashion for all rotors. It increases sharply, peaks, and then gradually decreases stabilizing at 2°. However, the rotor disk simulation shows a distinction between wing and tail rotors. For wing rotors, the collective pitch steadily increases to 6°. For tail rotors, there is no initial peak and the final solution stabilizes at around 2°, similar to the high-fidelity case. While it is difficult to pinpoint the exact cause of the differences in the control angles, they are likely related to differences in the aerodynamic solution of the rotors.

The change of delta-airloads with the iteration cycle is plotted in figure 15. For the rotor disk case, oscillations in the normal and chord force coefficients indicate that the rotor aerodynamic solution is less stable than that of the blade-resolved case. Although the oscillations are bounded and have a small amplitude, these changes may still affect the trim solution of the control angles, as seen in figure 14.

Table 6 compares the final thrust C_T and torque C_Q coefficients obtained. Once again, the results are averaged over the last rotor revolution for blade-resolved simulation, and over the last 5000 pseudo-time steps for the rotor disk simulation. In contrast to airplane mode, there is no systematic bias towards overprediction or underprediction of the results. The largest discrepancies in thrust coefficient, up to 6 %, occur for rotors located closer to the fuselage, with an overprediction for rotors 5-6 and an underprediction for rotors 7-8. Every rotor produces roughly the same amount of thrust, although there may be slight variations caused by mutual interferences that change the inflow. It is worth noting that the rotor disk model fails to accurately predict the torque coefficient. For rotors 3-4 and 5-6, the percentage change can amount to up to 23 % of the blade-resolved solution. This number is reduced to 10 % for rotors 1-2 and further down to 6 % for rotors 7-8. The high-fidelity solution predicts similar values of torque coefficient for all rotors. In the mid-fidelity solution, wing rotors yield similar torque coefficients, with minor variations, and all have a tendency to be overestimated. On the other hand, tail rotors present lower torque coefficients that are underpredicted in comparison to the high-fidelity case.

The aerodynamic loading is visualized through rotor maps

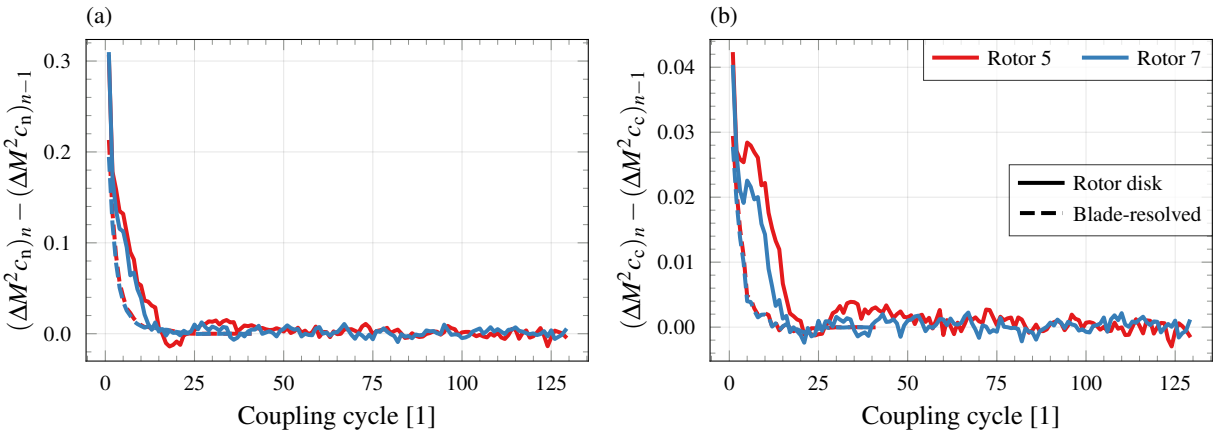

Figure 15: Convergence history of the delta-airloads approach in helicopter mode represented as the change between iterations for the (a) sectional normal force coefficient $M^2 c_n$ and (b) chord force coefficient $M^2 c_c$. The results are expressed in airfoil axes.

Table 6: Converged thrust and torque coefficients for the rotors in helicopter mode as predicted by rotor disk and blade-resolved simulations.

	Rotor disk		Blade-resolved		Percentage change	
	$C_T \times 10^2$ [1]	$C_Q \times 10^3$ [1]	$C_T \times 10^2$ [1]	$C_Q \times 10^3$ [1]	Thrust [%]	Torque [%]
Rotor 1	3.297	−7.344	3.378	−6.575	−2.42	11.69
Rotor 2	3.272	7.284	3.382	6.573	−3.26	10.82
Rotor 3	3.437	−7.669	3.298	−6.356	4.21	20.66
Rotor 4	3.411	7.605	3.296	6.367	3.47	19.44
Rotor 5	3.446	−7.690	3.250	−6.269	6.05	22.67
Rotor 6	3.381	7.547	3.257	6.285	3.82	20.09
Rotor 7	3.123	−5.957	3.305	−6.354	−5.49	−6.26
Rotor 8	3.161	6.021	3.298	6.370	−4.18	−5.48

of the normal force coefficient $M^2 c_n$ and chord force coefficient $M^2 c_c$ in figures 16 and 17, respectively. Disk planes are viewed from above and divided into four quadrants of $\psi = 90°$. The loads vary incrementally from the root to the tip due to a higher dynamic pressure. For an isolated hovering rotor, the loads are independent of the azimuthal position. In this case, aerodynamic interactions with other components break the symmetry. The way those are captured by the high- and mid-fidelity approaches is different. The high-fidelity solution is able to capture tip vortices that alter the flow field near the tip. This is observed as peaks in the normal and chord force coefficients at the edge of the rotor. Wake-tail interactions occur for rotors 7-8 after their blades pass over the horizontal tail at an azimuth angle of $\psi = 45°$, and are reflected as sharp rises of the normal and chord force coefficients. The key difference in capturing aerodynamic interactions lies in the fact that, for rotor disk simulations, the tip vortices are replaced by an axisymmetric ring-vortex sheet. The normal force coefficient peaks are no longer localized at the tips for every azimuthal position. Instead, they are localized near the regions of overlap between the rotors —for example, the left side for rotor 1, the right side for rotor 5, and both for rotor 3. The chord force coefficient distribution is overpredicted across the entire rotor disk. As opposed to airplane mode, no areas of negative lift are observed. This is because the inflow angle ϕ is lower. On the one hand, the rotor rotational speed Ω is greater; on the other hand, the axial flow through the rotor is only due to the induced velocity, without the freestream component —see equation 9. The resulting angle of attack is positive for every radial and azimuthal position.

A comparison of the normal and chord force distributions per unit span is presented in figure 18. The results indicate that the rotor disk model overpredicts the normal force for wing rotors over a large portion of the span, from the root to $r = 0.9R$. The agreement for tail rotors is relatively better. Beyond that section, the blade-resolved solution experiments a surge in the normal force due to the upwash created by the tip vortex, which the disk model fails to predict. The chord force is similarly overpredicted for wing rotors, which explains the higher torque coefficients obtained in table 6.

In helicopter mode, the trim quantities included for the trim task in CAMRAD II are the vertical force F_z and pitching moment M_y in airframe axes. An additional simplification was considered: the forces and moments on the fuselage, wing, and tail were not factored into the calculations. Therefore, the solution is not influenced by any deflections of the control

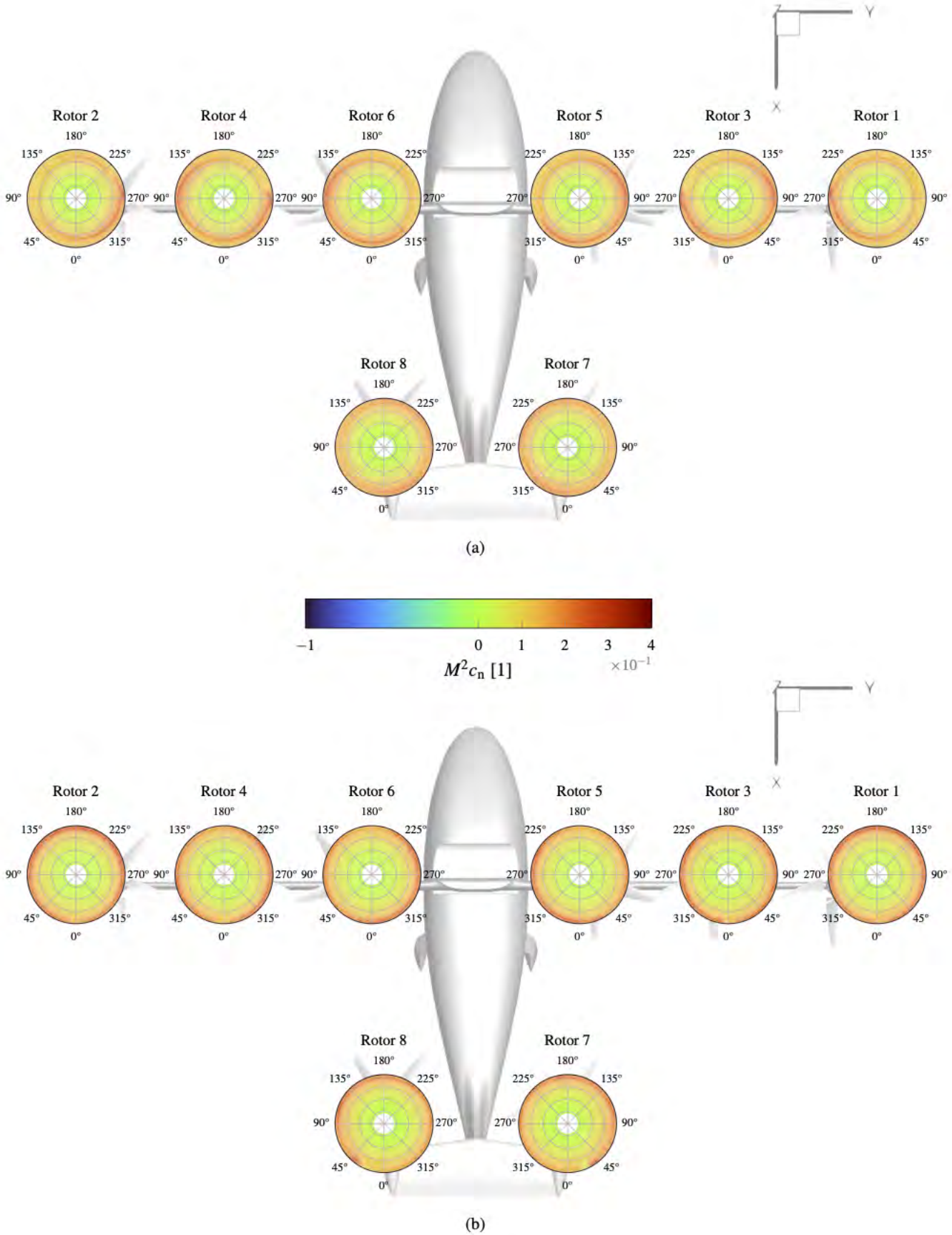

Figure 16: Sectional normal force coefficient M^2c_n distribution in helicopter mode: (a) rotor disk and (b) blade-resolved simulations.

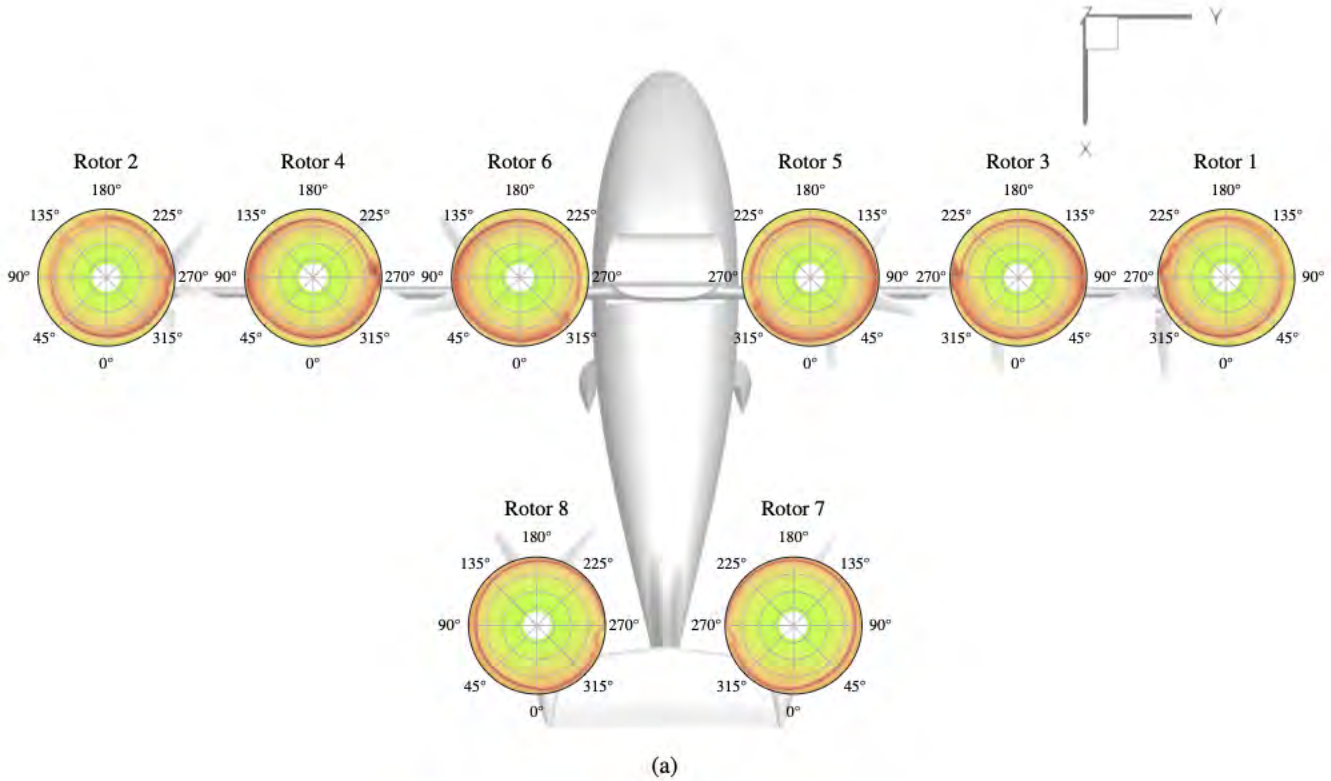

(a)

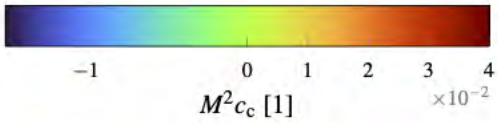

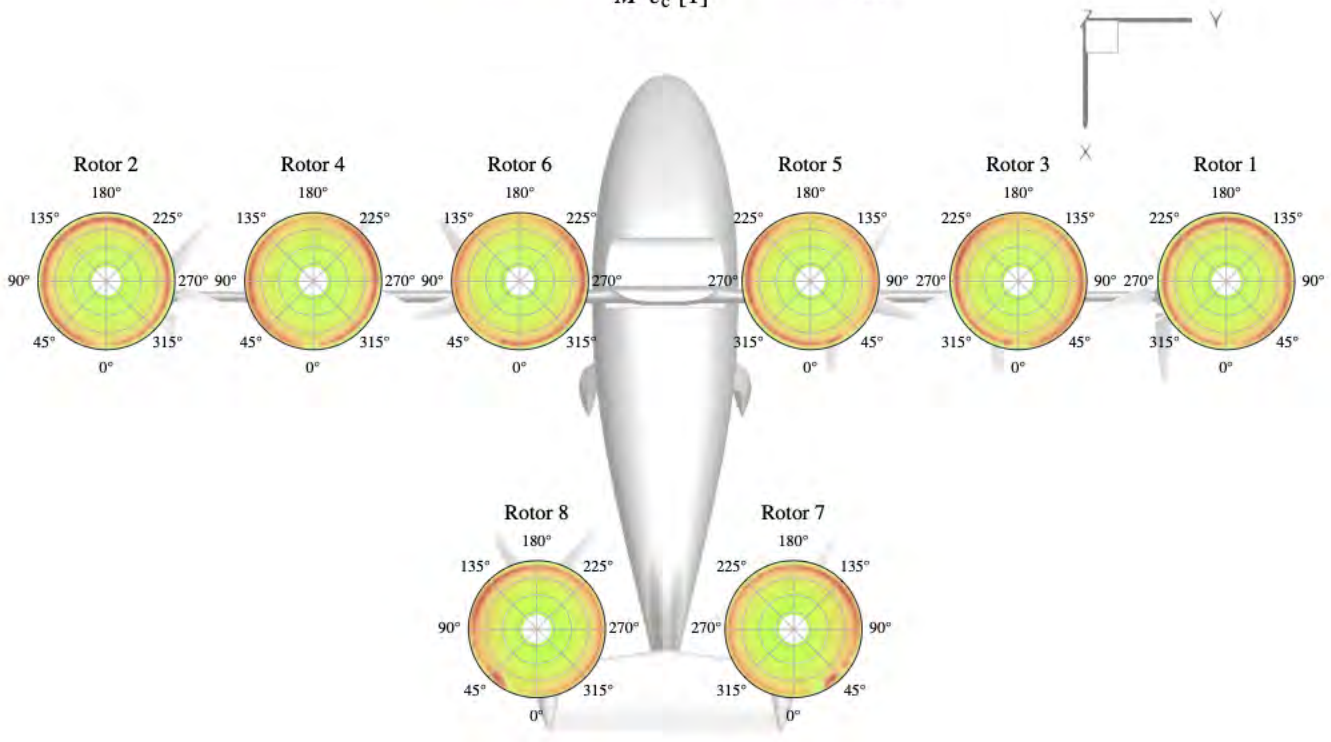

(b)

Figure 17: Sectional chord force coefficient $M^2 c_c$ distribution in helicopter mode: (a) rotor disk and (b) blade-resolved simulations.

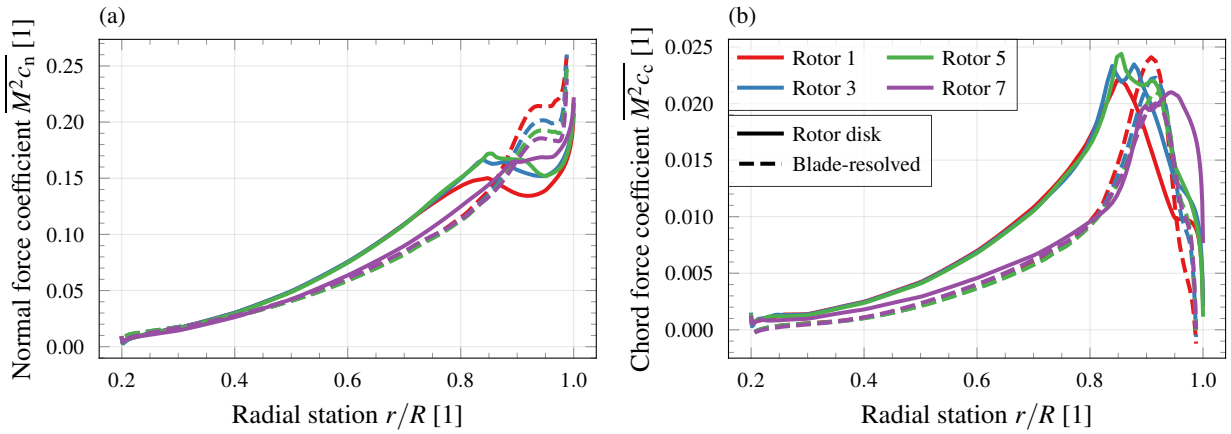

Figure 18: Evolution of mean sectional airloads with the radial station in helicopter mode: (a) normal force coefficient $M^2 c_n$ and (b) chord force coefficient $M^2 c_c$. The results are expressed in airfoil axes.

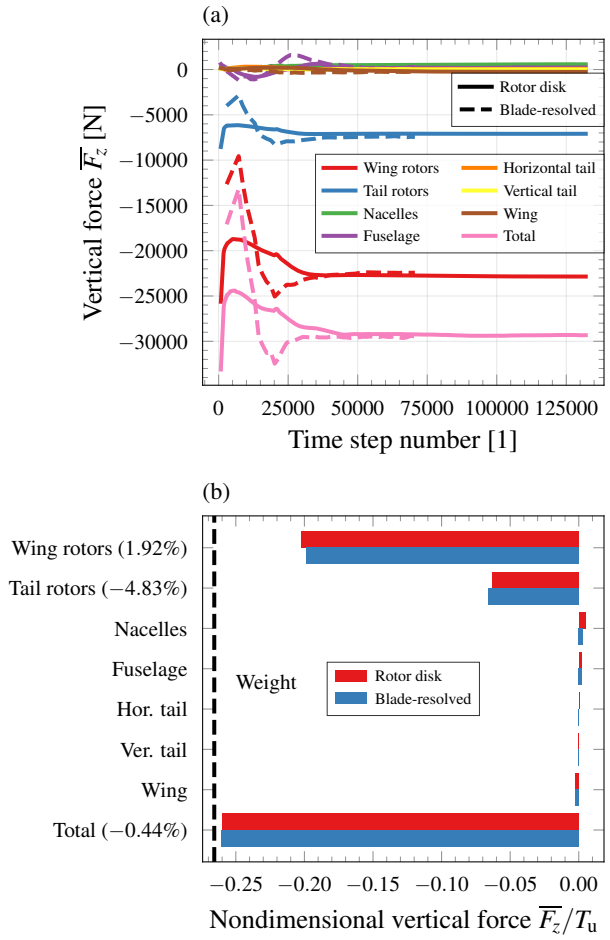

Figure 19: Trim solution for the aerodynamic forces in the vertical direction in helicopter mode: (a) evolution with the time/pseudo-time step number; (b) converged solution and percentage change.

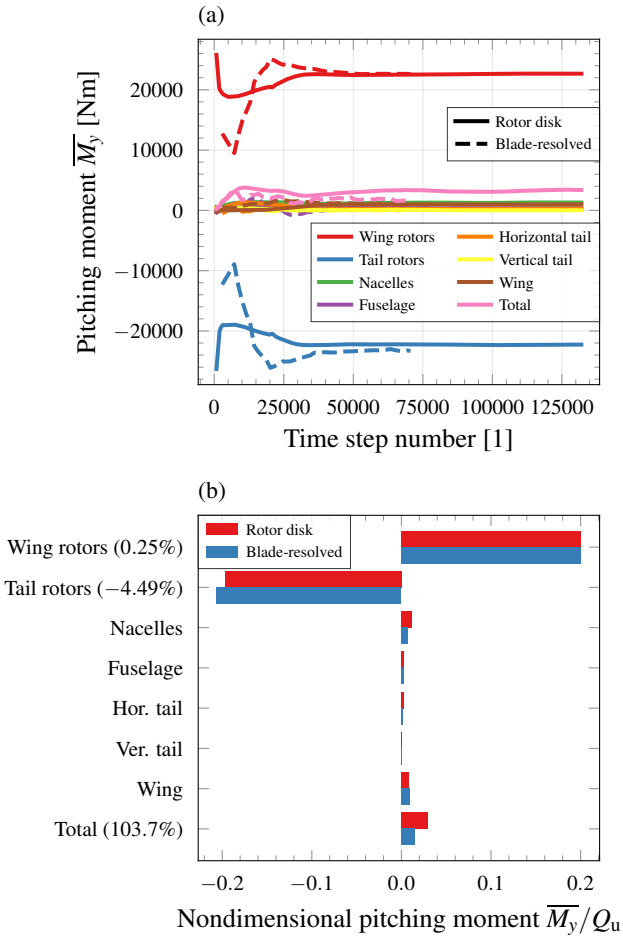

Figure 20: Trim solution for the pitching moment about the center of gravity in helicopter mode: (a) evolution with the time/pseudo-time step number; (b) converged solution and percentage change.

surfaces or the lack of exchange of integrated airloads. As the trim relies purely on the rotors' equilibrium, it will be more precise than in airplane mode. Figures 19 and 20 summarize the trim solution for the vertical force and pitching moment, respectively. In each figure, the top plot shows the evolution as the solution progresses in time or pseudo-time. The bottom plot shows a side-by-side comparison of the converged values obtained with the high- and mid-fidelity approaches. These are made dimensionless with characteristic magnitudes of thrust T_u and torque Q_u —see equation 10. The percentage change of components for which the blade-resolved solution is close to zero or accounts for less than 3 % of the total is not indicated.

Figure 19 shows the trim solution of the vertical force. The equilibrium along the z-axis is mainly established between the gravity component due to the weight and the thrust generated by the rotors. The contribution is divided approximately in the ratios 75/25 for wing and tail rotors. The percentage errors reported for those components are below 5 %. Although very small in magnitude compared to the rotors' thrust, a downforce is observed on the fuselage, nacelles, and horizontal tail. The contribution of these components is negligible, validating the assumption of neglecting them in the trim computation. The total aerodynamic vertical force cancels out the weight within a 2 % error.

Figure 20 illustrates the convergence of the pitching moment about the CG. The components involved in the moment balance are the wing and tail rotors. Since the CG is located between the wing and tail, wing rotors generate a nose-up moment that opposes the nose-down moment induced by tail rotors. The errors reported for those components are below 5 %, and the contribution of the other components accounts for less than 3 % of the total. Since the total pitching moment approaches zero, any errors on individual components will be relatively large relative to the trimmed value (103 %).

Wake geometry The wake structure is visualized via iso-surfaces of Q-criterion shaded by vorticity magnitude. Figure 21 shows a perspective front view of the vortex wake and demonstrates the crucial flow characteristics of the two models.

The rotor disk solution features ring-vortex sheets shed at the rotor tips. A similar structure is observed at the root. As previously discussed, this changes the flow field near the tip, where the effects of the tip vortices are important. Compared to airplane mode, the vortex sheets maintain their structure for a longer time due to the absence of axial freestream velocity. Beneath the rotors, worm-like formations are visible, which are thicker than those captured by the high-fidelity solution. This is true for the rotors 3-4 and 5-6 at a distance approximately one radius below the disk planes.

In the blade-resolved solution, each blade is tracked and resolved, resulting in individual tip vortices that form a clearly defined structure. These vortices follow a contracting helical path downstream until they reach a wake age of 360°, where they strike the wing or horizontal tail, become unstable, and lose their structure. The vortices remain near the rotors for a longer duration, which impacts their aerodynamics in two ways. Firstly, the blades encounter tip vortices trailed by preceding blades, leading to a localized loading increase near the tip (BVIs). Secondly, the rotor wakes interact with neighboring rotors. Wing rotors are placed in a staggered manner with minimal overlap when viewed from above. As the wake flows downstream, the blades of the rotor located below will encounter tip vortices generated by the rotor above. This is the case of outboard rotors 1-2 with middle rotors 3-4, and middle rotors 3-4 with inboard rotors 5-6. These rotor-rotor interactions affect their performance and individual airloads.

Figure 22 shows slices of vorticity magnitude taken at a y-plane containing the centerline of the wing leftmost rotor. These images provide valuable insights into the generation of vorticity. For the rotor disk case, vorticity is generated in the form of vortex sheets at the edges of the disk and transported downstream with the flow. In the blade-resolved case, boundary layers that contain vorticity formed in the upper and lower surfaces of the blade form wake shear layers upon leaving the trailing edge. These confluent boundary layers roll up to form the blade tip vortices. As seen in figure 22b, the shear layers travel downstream at a faster pace than the tip vortices.

Performance The performance of the rotors in hover is measured using the figure of merit (FM). It represents the ratio of ideal rotor power to actual power:

$$\mathrm{FM} = \frac{T v_i}{P}, \tag{12}$$

The FM is less than one due to viscous losses, three-dimensional effects, interferences from other lifting and non-lifting surfaces, etc.

Table 7 presents a summary of the results. For the blade-resolved case, the FM values for all rotors are similar, with rotors 5-6 being slightly lower. CAMRAD II free wake shows a tendency to overestimate the FM when compared to the blade-resolved solution. The percentage differences are approximately 11 % for rotors 1-2 and 3-4, and 15 % for rotors 5-6 and 7-8. This discrepancy is attributed to inaccurate modeling of interactional aerodynamics, which has a more significant

Table 7: Rotor performance in helicopter mode measured by the figure of merit. The results are obtained using: OVERFLOW blade-resolved simulations, OVERFLOW rotor disk modeling, and CAMRAD II free wake.

	Figure of merit FM		
	OVERFLOW/CAMRAD II		CAMRAD II
	Blade-resolved	Rotor disk	Free wake
Rotor 1	0.6640	0.6049	0.7413
Rotor 2	0.6649	0.6066	0.7413
Rotor 3	0.6605	0.6108	0.7397
Rotor 4	0.6609	0.6104	0.7397
Rotor 5	0.6549	0.6149	0.7544
Rotor 6	0.6549	0.6127	0.7544
Rotor 7	0.6648	0.6850	0.7662
Rotor 8	0.6659	0.6865	0.7662

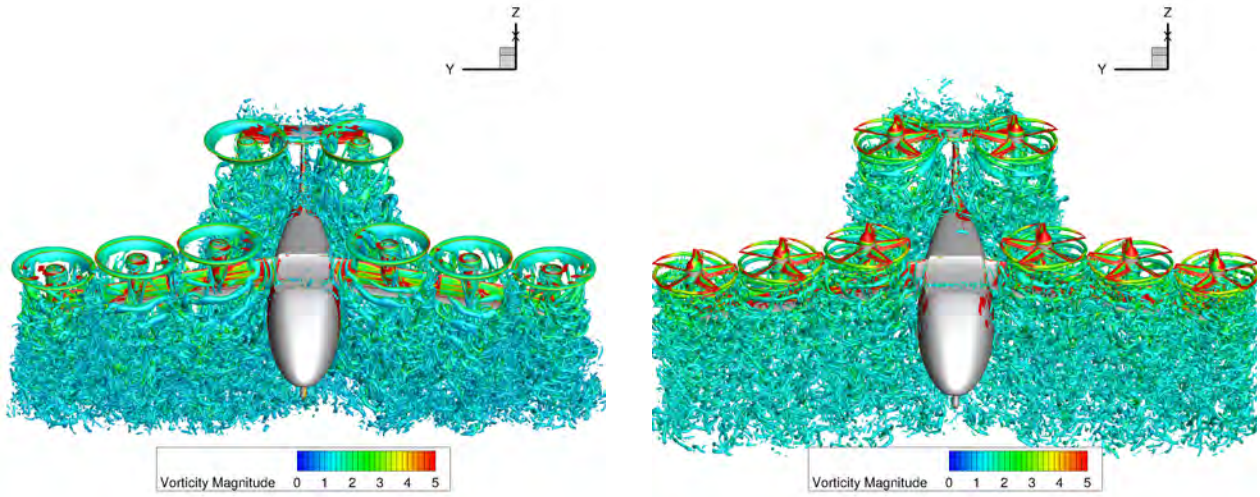

(a) (b)

Figure 21: Snapshot in time of the iso-surfaces of Q-criterion shaded with the vorticity magnitude in helicopter mode: (a) rotor disk and (b) blade-resolved simulations.

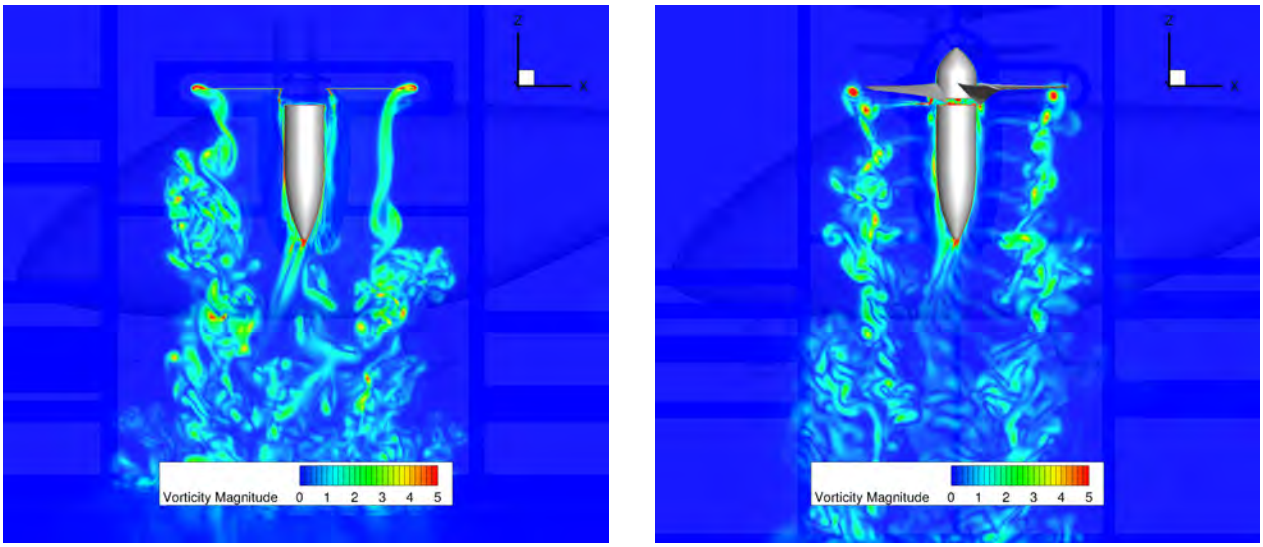

(a) (b)

Figure 22: Snapshot in time of a slice of vorticity magnitude taken at a y-plane containing the centerline of the wing's leftmost rotor in helicopter mode: (a) rotor disk and (b) blade-resolved simulations.

impact on rotors located closer to the fuselage. The use of the disk model allows for greater realism, as the aerodynamics of the components belong in the CFD part of the solution. This results in reduced relative differences, ranging between a 5-8 % overestimation for wing rotors, and a 3 % underestimation for tail rotors. It should be noted that the FM is a highly sensitive parameter to changes in thrust and torque coefficients. As such, the large percentage changes reported for the wing rotors in the torque coefficients explain the underprediction of the FM. Only the high-fidelity solution is capable of providing sufficiently accurate predictions of the FM.

CONCLUSIONS

A multi-fidelity analysis of NASA's tiltwing air taxi vehicle operating in airplane and helicopter mode has been performed. The flight conditions are representative stages of a typical UAM mission. High- and mid-fidelity CFD simulations using OVERFLOW were coupled with the comprehensive code CAMRAD II for more accurate calculations. The high-fidelity, time-accurate approach individually tracks and resolves each blade using body-fitted rotating grids. The mid-fidelity approach represents the rotor as an infinitely thin disk and uses source terms in the Navier-Stokes equations to model its effect on the airflow. A comparison of the trim solution, wake

geometry, and rotor performance was presented.

Simulations conducted in airplane mode showed a very good level of agreement between the high- and mid-fidelity solutions, with less than 5 % errors in the prediction of thrust and torque coefficients, and propulsive efficiency. Despite the simplifications inherent in the rotor disk model, it was able to capture the expected flowfield behavior with reasonable accuracy, including rotor-airframe aerodynamic interactions that decreased the thrust production of wing inboard rotors. The trim solution of the vertical force and pitching moment was obtained within a 6 % error. However, significant errors were found in the horizontal force trim. This was attributed to the detachment of the flow from the surface of the nacelles in the absence of spinners, leading to large pressure drag, i.e., the errors are not due to model limitations, but to differences in the geometries. The satisfactory agreement for this flight condition is partly due to its simpler nature, which involves no direct blade-vortex interactions. In contrast, during hover, the longer-lasting effects of the wake on the aerodynamics posed a greater challenge for the mid-fidelity solution. An accurate calculation of the wake is essential but the detailed description of the tip vortices is lost in favor of a ring-shaped vortex sheet representation of the wake. The delta-airloads approach revealed a less accurate aerodynamic solution, which was also reflected in the trimmed control angles. This mainly affected the prediction of the torque coefficient, with percentage differences above 20 %; and the figure of merit, with errors up to 15 %. However, the thrust coefficient errors as well as the errors associated with other longitudinal forces and moments were around 5 %, as evidenced by the trim solution.

The rotor disk model was shown to be an effective alternative to circumvent the complexity and large computational requirements associated with simulating unsteady flows of rotating blades. The cost of turnaround time was reduced by more than 80 %. This is particularly interesting for optimization applications or parametric studies, where this approach can be used as a surrogate model of the physical moving blades.

Future efforts will be directed toward analyzing the tiltwing vehicle in transition flight with proper balancing of the forces and moments.

ACKNOWLEDGMENTS

This work is supported by the Revolutionary Vertical Lift Technology (RVLT) Project (PM: Susan Gorton; TL: Brian Allan). The computations utilized the Pleiades, Electra, and Aitken supercomputers at the NASA Advanced Supercomputing Division. The authors would like to thank Wayne Johnson, Chris Silva, and Brian Allan, for helpful discussions.

REFERENCES

1. W. Johnson and C. Silva, "NASA Concept Vehicles and the Engineering of Advanced Air Mobility Aircraft," *The Aeronautical Journal*, vol. 126, no. 1295, pp. 59–91, 2022.

2. P. Ventura Diaz and S. Yoon, "High-Fidelity Simulations of a Quadrotor Vehicle for Urban Air Mobility," in *AIAA Paper 2020–0152*, San Diego, CA, January 2020.

3. P. Ventura Diaz, W. Johnson, J. Ahmad, and S. Yoon, "Computational Study of the Side-by-Side Urban Air Taxi Concept," in *VFS 75th Annual Forum*, Philadelphia, PA, May 2019.

4. P. Ventura Diaz, D. Garcia Perez, and S. Yoon, "Computational Analysis of a Quiet Single-Main Rotor Helicopter for Air Taxi Operations," in *VFS 78th Annual Forum*, Fort Worth, TX, May 2022.

5. J. U. Ahmad and N. M. Chaderjian, "High-Order Accurate CFD/CSD Simulation of the UH60 Rotor in Forward Flight," in *AIAA Paper 2011–3185*, Honolulu, HI, June 2011.

6. N. M. Chaderjian, "Advances in Rotor Performance and Turbulent Wake Simulation Using DES and Adaptive Mesh Refinement," in *Seventh International Conference on Computational Fluid Dynamics (ICCFD7)*, no. ARC-E-DAA-TN5574, Big Island, HI, July 2012.

7. D. D. Boyd, "Rotor/Fuselage Unsteady Interactional Aerodynamics: A New Computational Model," Ph.D. dissertation, Virginia Polytechnic Institute and State University, 1999.

8. I. Fejtek and L. Roberts, "Navier-Stokes Computation of Wing/Rotor Interaction for a Tilt Rotor in Hover," in *AIAA Paper 91-0707*, Reno, NV, January 1992.

9. L. A. J. Zori, S. R. Mathur, and R. G. Rajagopalan, "Three-Dimensional Calculations of Rotor-Airframe Interaction in Forward Flight," in *American Helicopter Society 48th Annual Forum*, Washington, D.C, June 1992.

10. M. S. Chaffin and J. D. Berry, "Helicopter Fuselage Aerodynamics Under a Rotor by Navier-Stokes Simulation," in *American Helicopter Society 51st Annual Forum*, Fort Worth, TX, May 1997.

11. J. U. Ahmad, "Application of Rotor Disk Model in the OVERFLOW CFD Code," NASA, Tech. Rep. NASA/TM-2022-0005496, April 2022.

12. D. Garcia Perez, P. Ventura Diaz, and S. Yoon, "High-Fidelity Simulations of a Tiltwing Vehicle for Urban Air Mobility," in *AIAA Paper 2023-2282*, National Harbor, MD, January 2023.

13. T. Pulliam, "High Order Accurate Finite-Difference Methods: as seen in OVERFLOW," in *AIAA Paper 2011–3851*, Honolulu, HI, June 2011.

14. W. Chan, R. Gomez, S. Rogers, and P. Buning, "Best Practices in Overset Grid Generation," in *AIAA Paper 2002–3191*, St. Louis, MO, June 2002.

15. W. Johnson, “Rotorcraft Aerodynamics Models for a Comprehensive Analysis,” in *American Helicopter Society 54th Annual Forum*, Washington, D.C., May 1998.

16. R. Haimes and J. Dannenhoffer, “The Engineering Sketch Pad: A Solid-Modeling, Feature-Based, Web-Enabled System for Building Parametric Geometry,” in *AIAA Paper 2013–3073*, San Diego, CA, June 2013.

17. R. Tramel, R. Nichols, and P. Buning, “Addition of improved shock-capturing schemes to OVERFLOW 2.1,” in *19th AIAA Computational Fluid Dynamics*, 2009, p. 3988.

18. P. Spalart, “Comments on the feasibility of les for wings, and on a hybrid rans/les approach,” in *The AFOSR International Conference on DNS/LES*. Greyden Press, 1997, pp. 137–147.

19. ——, “Strategies for turbulence modelling and simulations,” *International Journal of Heat and Fluid Flow*, vol. 21, no. 3, pp. 252–263, 2000.

20. M. Potsdam, H. Yeo, and W. Johnson, “Rotor Airloads Prediction Using Loose Aerodynamic/Structural Coupling,” *Journal of Aircraft*, vol. 43, no. 3, pp. 732–742, 2006.